Chapter 2
Controlled Synthesis and Surface Modification of Magnetic Nanoparticles with High Performance for Cancer Theranostics Combining Targeted MR Imaging and Hyperthermia

Jun Xie, Ning Gu, and Yu Zhang

Multifunctional inorganic nanoparticle (NP)-based theranostic agents are emerging as promising paradigm toward personalized nanocarrier or nanomedicine for the disease diagnosis and specific treatment [1–6]. Among these NPs, magnetic nanoparticles (MNPs) are very prominent since they have already been introduced into the clinical practice because of their unique physicochemical properties, such as high magnetic performance, excellent magnetically induced heating ability, and biocompatibility [7–11]. As conventional contrast imaging agents, MNP-based magnetic resonance (MR) imaging with substantial signal enhancement can help to locate active tumors and determine tumor stages, which is used for cancer early detection and diagnosis [7, 8, 10]. As a promising cancer therapy, MNP-induced targeted hyperthermia is mainly based on the heat generation by magnetic materials exposed to an alternating current magnetic field (ACMF), which provides the minimal damnification to deliver a therapeutic dose of heat specifically to cancerous regions [7, 8, 11]. To ensure an optimal strategy for cancer treatment in vivo, the integration of theranostics combining simultaneously magnetic resonance imaging (MRI) and efficient heat induction into a single nano-formulation has gained increased interest for researchers.

Developing the functional MNPs with high performance has become an important goal for efficient cancer theranostics. The high performance of MNPs, including superior magnetism, high magnetically induced heating effects, favorable biocompatibility, accurate targeting ability, and long circulation, is optimized by the controlled synthesis and surface functionalization. This is a rather challenging issue. In this regard, we will begin our review with the goal of describing controlled synthesis and surface modification of the MNPs with high performance, giving a

---

J. Xie • N. Gu • Y. Zhang (✉)
State Key Laboratory of Bioelectronics, Jiangsu Key Laboratory for Biomaterials
and Devices, School of Biological Science and Medical Engineering,
Southeast University, Nanjing 210096, People's Republic of China
e-mail: zhangyu@seu.edu.cn

Z. Dai (ed.), *Advances in Nanotheranostics II*, Springer Series
in Biomaterials Science and Engineering 7, DOI 10.1007/978-981-10-0063-8_2

background on the advantages of these high-quality MNPs and the advanced synthetic methods currently under investigation. We will then conclude with a discussion of current clinical applications of the MNPs, especially in cancer targeted MR imaging and hyperthermia in vivo, and get a perspective of MNP-mediated cancer theranostics strategy.

2.1 Controlled Synthesis and Surface Modification of MNPs with High Performance

In the last decades, much research has been dedicated to the synthesis of MNPs because the synthesis directly determines the physical properties of MNPs, including the composition, magnetism, size distribution, and morphology [12–15], which are fundamental for further biomedical applications. Generally, the synthesized bare MNPs are rapidly cleared from the blood circulation when passing through the biological defense system and vascular barriers. So introducing a surface modification, such as amphiphilic molecules, bifunctional polymeric ligands, or biomolecules, can provide a stabilizing layer that prevents MNP agglomeration and enhances colloidal stability, which is crucial requirement for almost any biomedical application of MNPs [16–19]. In the practical clinical application, the development of new types of MNPs with high performance, such as advanced MR contrast molecular imaging and magnetic heat generation ability, and prominent magnetic attractive forces for the transportation and movement of biological objects is particularly important. It will bring potential advantages and opportunities afforded by MNPs as platform materials for theranostics.

2.1.1 Conventional Synthesis of MNPs

Developing functional MNPs with high performance has become an important goal for chemists due to the chemical processes involved in the controlled synthesis and surface functionalization. During the last decades, many publications have described efficient synthetic routes to MNPs with different compositions and phases, including iron oxide pure metals (e.g., Fe_3O_4 and $\gamma-Fe_2O_3$) [20–23], magnetic dopant ferrite metals (e.g., $MnFe_2O_4$, $CoFe_2O_4$, and $ZnFe_2O_4$) [24–27], and metal alloy (e.g., FeCo and FePt) [28–31]. In conventional methods, such as coprecipitation, thermal decomposition, and/or reduction, microemulsion synthesis and hydrothermal synthesis techniques can all be directed at the synthesis of size-/shape-controlled, high-crystallinity, and monodisperse MNPs, which have been well documented and still described in progress [32–43].

The comparison of advantages and disadvantages of the abovementioned synthetic methods are briefly summarized in Table 2.1. As a whole, in terms of simplic-

Table 2.1 Summary comparison of conventional synthetic methods of MNPs

Synthetic method	Synthetic progress	Solvent, reaction temperature, and period	Size distribution	Shape control
Coprecipitation	MNPs are commonly made by hydrolysis/condensation of M^{2+} and Fe^{3+} ions by a base, usually NaOH, or $NH_3 \cdot H_2O$, in an aqueous solution or in reverse micelles [32–35]	Water, 20 ~ 80 °C, a few minutes	Relatively narrow	Not good
Thermal decomposition	MNPs can be made by reductive thermal decomposition of metal acetylacetonates or carboxylates in an organic phase in high-boiling organic solvents containing stabilizing surfactants [36–38]	Organic compound, 250 ~ 320 °C, a few hours	Very narrow	Very good
Microemulsion	A microemulsion is a thermodynamically stable isotropic dispersion of two immiscible liquids, where the microdomain of either or both liquids is stabilized by an interfacial film of surfactant molecules, which can be used as a nanoreactor for the formation of MNPs [39]	Organic compound, 20 ~ 50 °C, a few hours	Relatively narrow	Good
Hydrothermal synthesis	A process occurs spontaneously across the interface of metal linoleate and the water–ethanol solutions in a closed and high-pressure/high-temperature system. The MNPs generated at the interface are coated with a layer of linoleic acid, resulting in a spontaneous phase-separation process and the formation of hydrophobic MNPs [40–42]	Water–ethanol compound, 220 °C, a few hours	Very narrow	Very good

ity of the synthesis, coprecipitation is the preferred route and is suitable for mass production of MNPs, but it is difficult to control the synthesis of MNPs with uniform size distributions and various morphologies. Microemulsion methods can be used to synthesize the monodisperse MNPs; however, this method requires a complicated condition within a large amount of solvent, and the yield is very low. As an alternative, hydrothermal synthesis by a liquid–solid–solution reaction is a relatively suitable and little explored method to synthesize size- and shape-tunable

MNPs with high quality, but the reaction is in a closed and high-pressure system, hence lacking the ability for large-scale and practical application. In terms of size and morphology control of the MNPs, thermal decomposition seems the best method to obtain the high-performance MNPs (e.g., monodispersity, improved crystallinity, and larger magnetization) developed to date. In this regard, we will focus on the recent advance and advantage in the thermal decomposition synthesis of monodisperse MNPs with controlled size, shape, composition, and structure, and we will also try to present typical and representative examples for the discussion of this synthetic pathway and the corresponding formation mechanism.

2.1.2 Advantage of Synthesis of High-Quality MNPs by Thermal Decomposition

2.1.2.1 Formation Mechanism of Monodisperse MNPs by Thermal Decomposition

Recently, significant advances in preparing monodisperse MNPs have been made by the use of the thermal decomposition of organometallic precursors in high-boiling organic solvents in the presence of some stabilizing surfactants [36–38, 44–50]. The precursors usually include metal acetylacetonates [44, 45], metal cupferronates [46], or carboxylates [47]. Fatty acids [48], oleic acid [49], oleylamine [45], and hexadecylamine [50] are often used as typical capping surfactants. In MNP synthesis, a classical crystallization mode based on the supersaturation of solution is usually used to explain the crystal nucleation/growth kinetics, which plays a fundamental role in tailoring the MNPs with controllable sizes and shapes [44, 51]. The crystal process evaluated by variation of the monomer concentration can be described by using a La Mer model. With the supply of the precursor and surfactants, the monomer concentration was gradually increased and reached the minimum nucleation concentration. The reaction of molecular or atomic species rapidly takes the concentration of the precipitating species to above critical supersaturation. A large number of critical nuclei should be formed in a short interval of time, and the ensuing spontaneous nucleation that reduces the monomer concentration was rapidly decreased to below the nucleation threshold, at which stage the existing nuclei grow simultaneously at the same rate without production of fresh nuclei. When no new monomers were supplied in the reaction solution, the monomer was continuously consumed for subsequent particle growth, finally leading to the formation of monodisperse nanoparticles [44, 51].

2.1.2.2 Size Effects

One important parameter for high performance of MNPs is their appropriate size. As the MNP size decreases, their surface effect becomes more pronounced due to the increased volume fraction of surface atoms within the whole nanoparticle, which is reflected in reduced symmetry for the chemical surroundings of magnetic metal cations at the surface by the incomplete coordination [52–54]. Consequently, the surface magnetic structure is greatly different from that in the body of MNPs, and the magnetic interactions in the surface layer could have a notable effect on the magnetic properties of the MNPs [52, 55–57]. Generally, naturally ferromagnetic MNPs undergo a transition from multi- to single-domain magnetic structure as their size is reduced to below 80 ~ 90 nm. Further size reduction to less than 20 nm, the individual MNPs behave as a single magnetic domain and exhibit negligible remanence and coercivity, leading to their predominant superparamagnetism, which plays a critical role in practical applications [58]. In addition, the appropriate size of MNCs is highly related to their capabilities for effectively overcoming the biological defense system and vascular barriers in vivo. For example, MNPs with a large hydrodynamic diameter (e.g., >100 nm) are readily taken up by the mononuclear phagocyte system (MPS) and occur primarily in the liver and spleen [52, 59], while very smaller particles (e.g., <10 nm) may "leak" from the larger pores of fenestrated vascular networks or first-pass elimination by the kidney [35]. Hence, the MNPs with sizes of 10 ~ 100 nm can escape from phagocytes and travel through blood vessels with a reasonably high blood half-life (>1 h) [52, 60]. These relatively small-sized MNPs can have enhanced permeability and retention (EPR) effects at the target tissues because they can easily pass through the larger fenestrations of the blood vessels in the vicinity of cancerous tissues in vivo [61, 62].

Monodisperse ferrite MNPs with desired size distribution were usually made by varying reaction conditions or by seed-mediated growth in a high-temperature decomposition synthesis [63–65]. For instance, it was found that separation of nucleation and growth in time is required for the formation of monodisperse MNPs. By varying synthetic parameters including precursors, solvents, amount of surfactants, and heating rate of the solution, the MNP size from 2 to 9 nm could be controlled with 1 nm accuracy [63], as shown in Fig. 2.1a. Additionally, a practical and relatively simple approach for the synthesis of crystalline MNP controllable size is seed-mediated crystal growth, which is proved to be a reproducible method and is of great fundamental and technological interest for researchers [64]. The process firstly involves high-temperature (usually up to 300 °C) reaction of metal acetylacetonate with 1,2-hexadecanediol and surfactants (such as oleic acid (OA) and oleylamine (OAm)), in making monodisperse smaller-sized MNPs. With the smaller MNPs as seeds, the larger MNPs can be successfully synthesized by seed-mediated growth (Fig. 2.1b). The process can result in MNPs with desired size distribution and is readily suitable for mass production.

2.1.2.3 Shape Effects: From 0-D Nanocrystals to 3-D Nanoclusters

Recently, keen interests have been expanded into controlling the shape of nanostructure and also into understanding the correlations between the material properties, function, and its shape [65–74]. These shape–function relationships are particularly interesting for magnetic nanostructure, because the physical and chemical properties of the nanostructure are highly dependent on the material

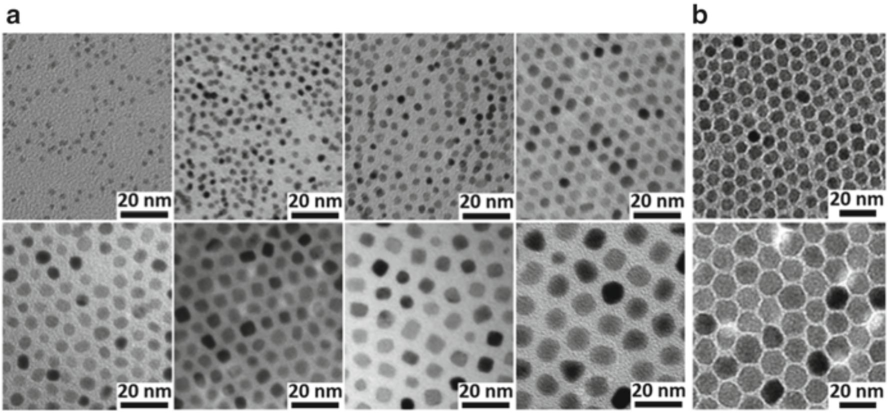

Fig. 2.1 (**a**) TEM images of synthesized MNPs of size from 2 to 9 nm by varying synthetic parameters (Reprinted with permission from Ref. [63]. Copyright 2007, American Chemical Society). (**b**) TEM bright field images of synthesized MNPs used by seed-mediated growth (Reprinted with permission from Ref. [64]. Copyright 2004, American Chemical Society)

morphology, which can enhance the prospects for promising application in a wide range of scientific and technological fields, including magnetism, electronics, catalysis, biochemistry, and medicine [44, 45, 65–74]. The shape of magnetic nanostructure can be simply classified by their dimensionality. Generally, 0-D magnetic nanostructures (e.g., spheres, cubes, and polyhedrons) are the most basic motifs among shaped nanocrystals.

The improved understanding and investigation of the shape-controllable synthetic mechanism is reviewed here. Generally, the essence of shape controlling of nanostructures is tuning the growth rate in specific directions, which is governed by the intrinsic surface energy and the monomer concentration in the crystal growth process. For magnetic ferrite nanocrystals, the typical spinel structure is based on a face-centered cubic model with three low-energy facets, {100}, {110}, and {111} (Fig. 2.2a) [44, 45, 65]. The {100} planes show the lowest surface energy, while the {111} planes have the highest [65]. In this regard, the choice of appropriate surfactant remains an important challenge in the shape controlling of nanocrystals, because the surfactant can selectively bind to specific crystal facets with lower energy, and tunes their growing rate. The OA as a typical capping surfactant is used to stabilize the formation of magnetic nanocrystals in a decomposition reaction of metal precursors. For example, by adjusting OA/OAm ratios, the synthesized spherical, cubical, and starlike nanocrystals were systematically investigated (Fig. 2.2b) [65]. The OA with its carboxylic group bound strongly onto certain crystal facets of initial nuclei, forming a stabilizing layer. Whereas, the OAm with an amine group as a crucial reducing agent here has relatively weak binding onto the crystal surface. It was evident that the various crystal planes are well capped and stabilized and the differential growth of crystal facets is negligible when OA was sufficient, thus leading to uniform spherical shape. Contrastively, when insufficient

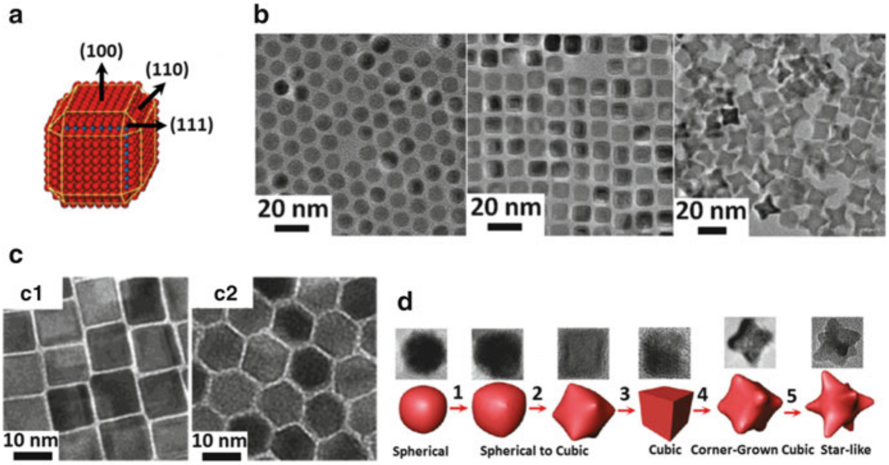

Fig. 2.2 (**a**) The face-centered cubic (*fcc*) models of typical spinel structure with three low-energy facets (Reprinted with permission from Ref. [44]. Copyright 2011, American Chemical Society). (**b**) TEM images of synthesized spherical, cubical, and starlike MNPs (Reprinted with permission from Ref. [65]. Copyright 2013, American Chemical Society). (**c**) TEM images of the synthesized cubelike and polyhedron-shaped MNPs (Reprinted with permission from Ref. [66]. Copyright 2004, American Chemical Society). (**d**) Schematic illustration of the shape evolution mechanism of MNPs (Reprinted with permission from Ref. [67]. Copyright 2009, American Chemical Society)

amounts of OA were used, it induced the preferential stabilization on the {100} crystal facets with lower energy, and grew along the [75] or [76] direction, resulting in the formation of cubical and starlike nanocrystals with the terminated {100} facets [65]. Another study had also described that the shape of magnetic nanocrystals was tuned by varying the amount of stabilizers to metal precursors [66]. When the surfactant/precursor ratio was smaller than 3:1, the nanocrystals were nearly spherical with no well-defined facets, and increasing the ratio to 3:1 yields cubelike particles. If the nanocrystals were further prepared using seed-mediated growth, the polyhedron-shaped particles were obtained (Fig. 2.2c) [66].

Besides the surface energy-mediated surfactant effects, the monomer concentration synchronously tailors the morphology of magnetic nanocrystals [67]. A few initial "crystal units" might appear at the stage from the decomposition of precursor, in which the monomer concentration was continually increased, gradually leading to the formation of spherical nanocrystals. Generally, most of spherical nanocrystals might keep growing to form the cubic shape until the excess monomers in the solution were nearly exhausted and their concentration reduced to the equilibrium concentration. The definite formation of nanocrystals was dependent on the reaction temperature, heating rate, and aging time. As the continuous consumption of the monomer, a limited number of nuclei could grow to form large nanocubes. The concentration of defects and surface energy in individual crystallites decreased in going from the corners, to the edges, to the crystal faces of nanocubes. Thus, the growth preferences for different sections of nanocubes are the corners, the edges, and the faces, respectively [67]. The shape evolution with increasing aging time from spherical to the intermediate spherical-to-cubic, to cubic, and eventually to corner-grown nanocube morphology was shown in Fig. 2.2d [67].

In addition, successes in similar monodisperse magnetic nanostructures with corner-grown shape synthesized by thermal decomposition of iron oleates had been reported by Gao and co-workers [68]. They reported that introducing the chloride anions as the capping agent had an important role in the formation of the nanostructures with specific morphology. The size-controllable octapod magnetic nanostructures consisting of uniform four-armed starlike iron oxide particles with high yield were prepared in the presence of NaCl (Fig. 2.3a) [68]. One possible forming mechanism was that the chloride ions were selectively bound to iron ions exposed on the high-index facets (probably [311]) during the nanostructure growth [68].

Except for 0-D magnetic nanocrystals, 1-D nanostructures could also be interesting for studying structural anisotropy, magnetic properties, and their corresponding biomedical applications [69–71]. For example, dextran-encapsulated 1-D chains of iron oxide nanoworms showed enhanced retention effects at the tumor sites and increased blood circulation time [69]. Furthermore, anisotropic 1-D nanostructures can interact and penetrate cellular membranes more efficiently, which makes them to be good candidates as drug carriers [70]. Herein, Bao et al. reported a simple colloidal synthesis method for preparing the single-crystalline 1-D magnetic nanorods by the iron oleate precursor thermal decomposition, where the aspect ratios of the iron oxide nanorods could be tuned by changing reaction temperatures (Fig. 2.3b) [71]. They found that the oleic ligand on the iron oleate complex was proposed to have played an important role in directing the elongated nanostructure formation at

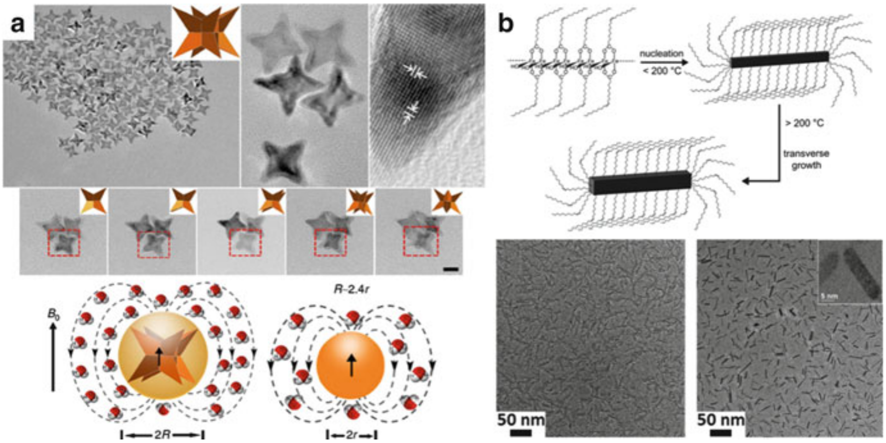

Fig. 2.3 (**a**) TEM, higher magnification, and tilted TEM images of octapod MNPs (inset: geometric model). Scale bar, 100 nm, and schematic cartoon of ball models of octapod and spherical MNPs with the same geometric volume. Scale bar, 20 nm (Reprinted with permission from Ref. [68]. Copyright 2013, Macmillan Publishers Ltd). (**b**) Proposed growth mechanism and TEM images of iron oxide nanorods (Reproduced from Ref. [71] by permission of The Royal Society of Chemistry)

the nucleation stage below 200 °C [71]. When further raising the reaction temperature, the structure directing oleate group may start to desorb and decompose. The transverse growth of the nanorods would then outgrow the longitudinal one, which also served to decrease the surface energy and structure anisotropy [71].

Unlike 0-D or 1-D nanostructures, recent synthetic studies of 3-D magnetic nanostructure have mostly focused on the "clusters" or "assemblies." Their peculiar structures of 3-D nanoclusters based on crystal aggregation have been shown theoretically and experimentally to be able to influence their magnetic properties, which are used as efficient mediators for MRI and hyperthermia in cancer treatment [72]. Furthermore, the clusters of magnetic nanoparticles with multiple crystal facets tend to have a larger surface area than individual nanocrystals [73], which may play a dominant role in catalytic research and application. In nanocrystal synthesis, a classical crystallization mode based on the supersaturation of solution is usually used to explain the crystal nucleation/growth process of nanocrystals with controllable sizes and shapes [74]. In contrast, another significant mechanism named nonclassical "oriented attachment" is recently proposed, where nanoparticles with common crystal orientations directly combine together to form larger ones [77]. The aggregation-based crystal growth theory shows its specific characteristics and roles in the formation of larger and irregular nanoclusters.

The strategy of forming magnetic nanoclusters by oriented attachment of individual nanocrystals has the advantage of controllably increasing the magnetization while retaining the superparamagnetic characteristics. Recently, Gupta's group reported novel superparamagnetic 3-D "nanoflowers," which composed of self-assembled spherical and rodlike colloidal nanocrystals (Fig. 2.4a) [73]. The formation of such nanoclusters was likely because of the burst boiling accompanied by a temperature drop when injecting a small amount of hexane during the heating and aging steps. The effects might slow down the growth of the nuclei and promote their assembly to form clusters by the particle coalescence (from interaction between the nuclei) or oriented attachment to decrease the surface energy [73]. Similarly, Zhang's group had synthesized highly ordered, self-assembled 3-D nanoclusters with sharp and obtuse edges, which were fabricated by controlling the nucleation/growth dynamics [65]. They found that shortening nucleation duration might bring a deficient nucleation and induce a rapid increase in monomer concentration, which accelerated subsequent growth process of nanocrystals, leading to the formation of the starlike nanocrystals with larger size. They are further oriented to assemble reciprocally, gradually forming initial "branched" nanoclusters to minimize the magnetostatic energy, owing to their size-dependent magnetic dipolar interaction [65]. Furthermore, the surface-defect-induced secondary growth of the "branched" nanoclusters might considerably improve their uniformity, resulting in the final "multibranched" nanoclusters with formation of sharp or obtuse edges [65]. They revealed the transformation of 0-D nanocrystals to 3-D nanoclusters as well as the shape evolution, which provide a synthetic strategy for shape-controlled nanostructure, as shown in Fig. 2.4b.

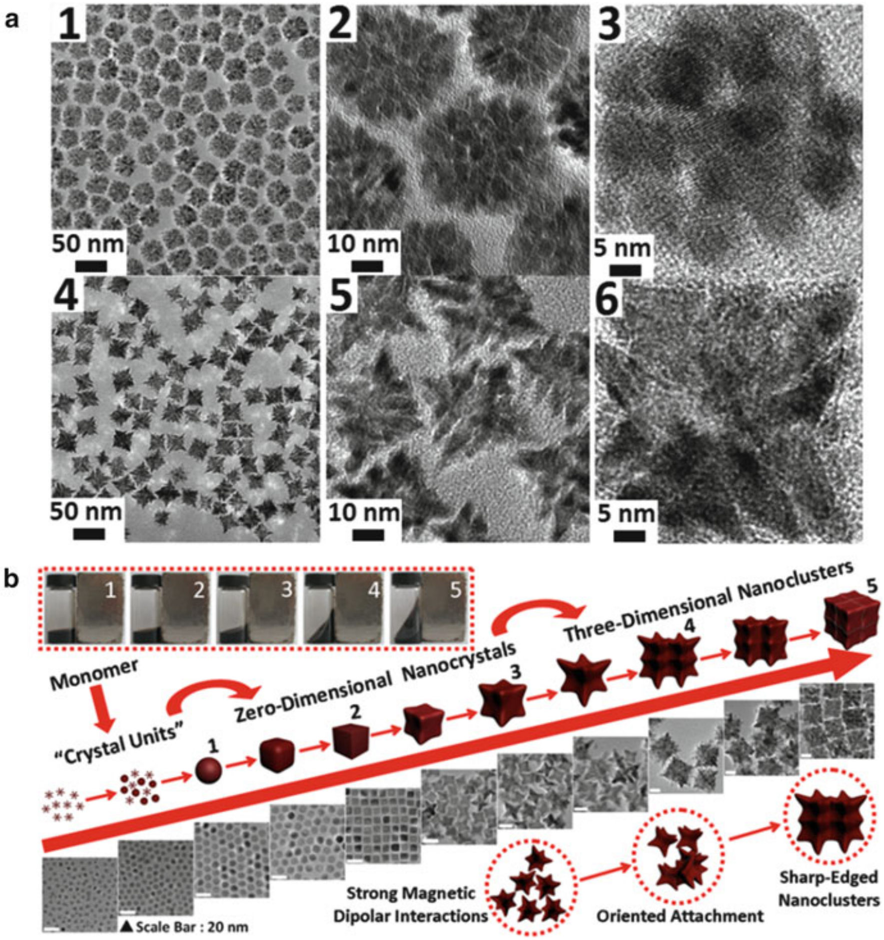

Fig. 2.4 (**a**) TEM images of 3-D self-supported (1–3) spherical and (4–6) cubic magnetic nanoclusters composed of intergrown spherical and rodlike MNPs, respectively (Reprinted with permission from Ref. [73]. Copyright 2009, American Chemical Society). (**b**) Schematic illustration of the transformation of 0-D magnetic nanocrystals to 3-D nanoclusters (Reprinted with permission from Ref. [65]. Copyright 2013, American Chemical Society)

2.1.2.4 Magnetic Metal-Dopant Effects

The magnetism of magnetic nanostructures can be greatly influenced by doping with magnetically susceptible elements. This strategy is demonstrated for the synthesis of binary ferrite MFe_2O_4 (M = Mn, Co, Ni, etc.) nanostructure with controllable sizes and shapes in which Fe^{2+} ions are replaced by other transition-metal M^{2+} dopants [24–26, 64–67, 78–80]. For inverse spinel Fe_3O_4 nanostructure, it has a crystal structure constructed of face-centered cubic packed lattice of oxygen atoms with the tetrahedral sites (T_d) occupied by Fe^{3+} ions and octahedral sites (O_h)

occupied by Fe^{3+} and Fe^{2+} ions [52]. Fe^{3+} has a d^5 configuration, and Fe^{2+} has a d^6 configuration with a high-spin state; the calculated total magnetic moment per unit Fe_3O_4 is 4 μ_B [52]. For metal-dopant substitution of ferrite MFe_2O_4, such as $MnFe_2O_4$, $CoFe_2O_4$, and $NiFe_2O_4$ nanostructure, the magnetic moments per unit can be estimated as 5 μ_B, 3 μ_B, and 2 μ_B under their electron spin configurations, respectively (Fig. 2.5a) [10]. It is worthwhile to note that the mass magnetization (M_s) value is highest for $MnFe_2O_4$ nanostructure (110 $emu \cdot g^{-1}$ MnFe) and decreases for Fe_3O_4 nanostructure (101 $emu \cdot g^{-1}$ Fe), which is proportionate to the magnetic moment values [10]. This doped $MnFe_2O_4$ nanostructure can also induce significant $T2$-weighted MR contrast-enhancement effects with the coefficient $r2$ of 358 $mM^{-1}s^{-1}$, which is more than two times higher than the values of conventional iron oxide-related MR contrast agents [10]. Significantly, a recent report of the successful Zn^{2+} doping leads to an extremely high magnetization value (175 $emu \cdot g^{-1}$) tuning and provides the larger MRI contrast effects ($r2 = 860$ $mM^{-1}s^{-1}$) (Fig. 2.5b) [78]. This increased MR contrast-enhancement capability of magnetic metal-doped nanostructures is advantageous, for example, for imaging-guided tumor diagnosis in vivo (See Sect. 2.2).

The high magnetization values of the metal-dopant nanostructure can also be used to achieve magnetically induced heat generation under an alternating current magnetic field (ACMF), which is evaluated by specific loss power (SLP) or specific absorption rate (SAR) values, the standard criterion for hyperthermia effects (defined as the thermal power dissipation divided by the mass of the magnetic material and the heat capacity of solution) [78, 81, 82]. For instance, the SLP value of 15 nm $(Zn_{0.4}Mn_{0.6})Fe_2O_4$ nanoparticles is 432 W g^{-1}, which is four times larger than that of Feridex (115 W g^{-1}) when measured under the identical conditions [78]. The high performance of Mn/Zn-doped ferrite nanoparticles plays a significant role in the thermal treatment of cancer and other diseases (See Sect. 2.3).

Except for the total magnetic moment increase, the metal-dopant substitution-induced novel core–shell structure may constitute an important strategy for achieving excellent magnetic properties drastically different from those of regular doped ferrite nanoparticles [79–81, 83]. Zhong's group recently reported a core–shell-structured ternary nanocube consisting of Fe_3O_4 core and Mn–Zn shells synthesized by controlling the reaction temperature in the absence of conventionally used reducing agents, as shown in Fig. 2.5c. The core–shell-structured nanocubes displayed unique magnetic properties, such as increased coercivity and field-cooled/zero-field-cooled characteristics by a combination of the core–shell composition, which was useful for magnetic and catalytic applications [79]. In addition, Cheon's group had designed some versatile core and shell combinations including $CoFe_2O_4$@$MnFe_2O_4$, $CoFe_2O_4$@Fe_3O_4, Fe_3O_4@$CoFe_2O_4$, and $Zn_{0.4}Co_{0.6}Fe_2O_4$@$Zn_{0.4}Mn_{0.6}Fe_2O_4$ with mutual coupling of magnetically hard and soft components (Fig. 2.5d) [80]. They took the advantage of the exchange coupling between a magnetically hard core and magnetically soft shell to tune the magnetic properties of the nanostructure and maximized the heat induction, which was a gauge of the conversion efficiency [80]. The coupled system could allow optimal tuning of magnetocrystalline anisotropy (K) values in particular, as well as M values, to achieve high SLP values while

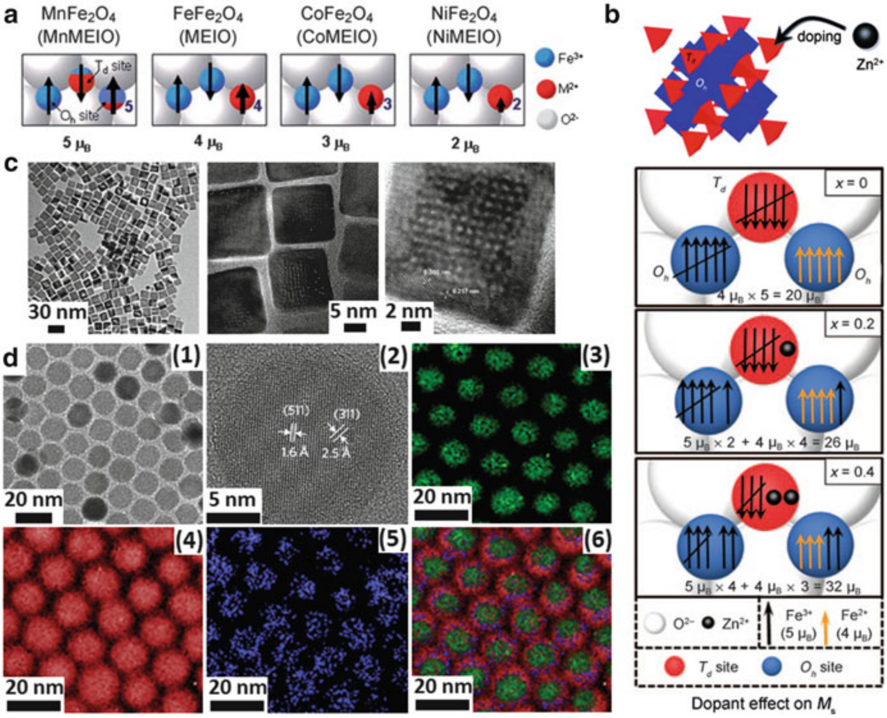

Fig. 2.5 (**a**) Magnetic spin structures of metal-doped MFe_2O_4 (M = Mn, Fe, Co, Ni) NPs (Reprinted with permission from Ref. [10]. Copyright 2007, Nature). (**b**) Zn^{2+}-doped magnetic spin alignment diagrams in spinel-structured $(Zn_xFe_{1-x})Fe_2O_4$ NPs (Reprinted with permission from Ref. [78]. Copyright 2009, John Wiley & Sons Ltd). (**c**) TEM images of morphologies of Mn–Zn ferrite core–shell nanocubes (Reprinted with permission from Ref. [79]. Copyright 2010, American Chemical Society). (**d**) TEM image (*1*), high-resolution TEM image (*2*) of core–shell $CoFe_2O_4$@$MnFe_2O_4$ NPs, and (*3–6*) the corresponding electron energy loss spectrum (EELS) mapped images: (*3*) Co-mapped image, (*4*) Fe-mapped image (*5*), Mn-mapped image, (*6*) and overlay image of (*3–6*) (Reprinted with permission from Ref. [80]. Copyright 2011, Macmillan Publishers Ltd)

maintaining the superparamagnetism (e.g., $CoFe_2O_4$@$MnFe_2O_4$, 2,280 W g^{-1}; $CoFe_2O_4$@Fe_3O_4, 1,120 W g^{-1}; $MnFe_2O_4$@$CoFe_2O_4$, 3,034 W g^{-1}; Fe_3O_4@$CoFe_2O_4$, 2,795 W g^{-1}; $Zn_{0.4}Co_{0.6}Fe_2O_4$@$Zn_{0.4}Mn_{0.6}Fe_2O_4$, 3,886 W g^{-1}) [80]. These optimized core–shell nanostructure with adequate biocompatibility could be a highly effective new nanoscale tool useful for magnetic hyperthermia therapy and other advanced nanobiotechnology applications, such as drug release, and thermal activation induced anticancer drug release carriers.

2.1.2.5 Metal Alloy

The magnetic metal alloy nanostructure (e.g., FeCo or FePt) fabricated by thermal decomposition synthesis is another example of magnetic nanostructures with high performance [28, 52, 63]. In these nanostructures, all the magnetic spins align parallel to the external magnetic field, so they typically have higher magnetic moments, leading to larger magnetocrystalline anisotropy and magnetization [52]. Take 7 nm-sized FeCo nanostructures for example; their magnetic moment was approximately 2.4 μ_B per magnetic atom, while that of Fe_3O_4 nanostructures was 1.3 μ_B per magnetic atom [28, 52]. These monodisperse FeCo nanostructures had an exceptionally high magnetization value of 215 emu · g^{-1} metal, and the coefficient *r2* value was determined to be 644 $mM^{-1}s^{-1}$, which was much larger than that of conventional Feridex contrast agents [28]. These advantages successfully endowed them with efficient *T1*-weighted MR imaging ability in vitro or in vivo.

2.1.3 Surface Modification of MNPs

2.1.3.1 Ligand Conjugation

Surface modification of MNPs discussed here is critical to improving their stability, biocompatibility, and functionality, which has widely received enormous attention in biomedical applications in vivo. Recently, a variety of ligand conjugation strategies for MNPs have been developed to give high colloidal stability in aqueous biofluids and to avoid aggregation which can occur under physiological conditions using different synthetic routes (Fig. 2.6) [20, 52, 84–96]. One commonly used method for surface coating is the physical adsorption of material onto the surface of

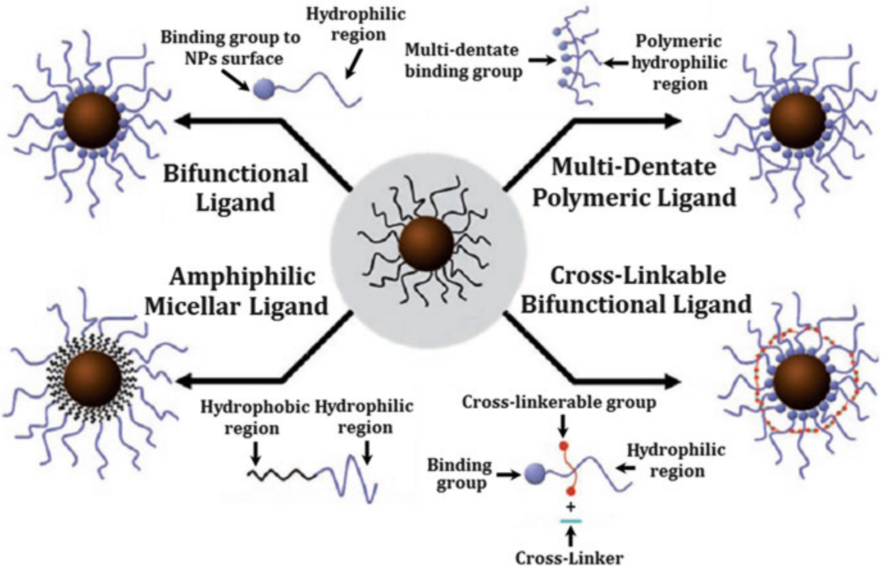

Fig. 2.6 Surface modification strategies for designing MNPs with high colloidal stability (Reprinted with permission from Ref. [52]. Copyright 2008, John Wiley & Sons Ltd)

the particle. Another such method to coat MNP surfaces also involves covalently or ionically bonding a polymer to the particle surface [84].

In general, as a conventional ligand, the biologically inert polymer chains have been used to modify MNPs for controlling the particle shape, size, and functionality that permits multiple applications. Polyethylene glycol (PEG) is one such polymer being explored for use in biological particle systems because of its solubility in water, low immunogenicity, biocompatibility, and fast clearance ability. The surface modification of MNPs with PEG, known as PEGylation, has been proposed for the improved stealth properties covered extensively in the literature [85, 86]; they include: (1) shielding the surface charge, increasing the hydrophilicity, and decreasing the interfacial free tension of the MNPs, which leads to reduced interaction and identification by opsonin proteins; (2) generating repulsive forces through the compression of flexible PEG chains on the surface of MNPs, which results in preventing specific binding to proteins; (3) and inhibiting phagocytosis by the reticuloendothelial system (RES), prolonging half-life in blood circulation, and promoting the EPR effect in vivo. To achieve the necessary stealth properties, the most suitable molecular weight of the PEG chain has been reported between 1,500 and 5,000 Da [86]. It is worthwhile to note that the direct one-step PEGylation of MNPs has the additional advantages of providing small and uniform MNPs [87–89]. As reported, PEGylated MNPs as small as from 4 to 9.8 nm had been prepared directly from monocarboxyl-terminated PEG through the covalent binding to the surface hydroxy groups by thermal decomposition of [Fe(acac)$_3$] in pyrrolidone and PEG [87]. The further MRI experiments performed on living rats demonstrated that the PEG-modified MNPs had long circulation time and very good biocompatibility and could potentially be used as MRI contrast agents. Many multifunctional PEG *ligands* have been commercially available for modifying MNPs. For instance, the MNPs were frequently coated with the combination of bifunctional PEG-silane [90–92]. The PEGylated MNPs had been synthesized by coating the MNPs first with a silane group using either amino propyl trimethoxy silane (APTMS) or amino propyl triethoxy silane (APTES) and then functionalized the amine terminal group with a carboxy-terminated PEG for attaching to targeting groups [90].

In addition, a challenge in developing therapeutic PEGylated MNPs conjugated with polypeptide or antibodies has recently shown a promising application. In order to increase the probability of the long-circulating PEGylated MNPs to the desired target, the MNP surface should be labeled with polypeptide or antibodies that specifically bind to surface epitopes or receptors on the target sites. These ligands have to be not macrophage recognizable and coupled to the surface of stealth carriers [84, 93]. In this regard, Chen's group had firstly modified iron oxide NP surface with PEG copolymer, making them water soluble and function extendable. These MNPs were then covalently conjugated with a near-infrared fluorescent (NIRF) dye (IRDye800) and a cyclic arginine–glycine–aspartic acid (RGD)-containing peptide c(RGDyK) for integrin $\alpha_v\beta_3$ targeting, which possessed excellent tumor integrin targeting efficiency and specificity as well as limited RES uptake for molecular MRI diagnostics [93]. It is to be observed that the antibody coupling has at least two drawbacks: the overall dimensions of the antibodies (ca. 20 nm) may cause MNPs to poorly diffuse through biological barriers in vivo, and their immunogenicity may evoke an immune response within an organism [84]. So the coupling of small non-immunogenic ligands to polymeric carriers should be noticed and investigated.

Besides PEG, other block copolymers, such as polyaniline or polystyrene, can also be used to coat MNPs by the oxidative polymerization in the presence of the oxidant ammonium peroxydisulfate [94–96]. For example, Asher et al. reported that single Fe_3O_4 MNPs (ca.10 nm) can be embedded in polystyrene spheres through emulsion polymerization to give stable superparamagnetic photonic crystals [95]. Zhang et al. had used this method for coating $MnFe_2O_4$ MNPs with polystyrene, yielding core–shell nanoparticles with sizes below 15 nm [96].

The use of cross-linkable small molecules as bifunctional ligands can also be advantageous since the cross-linking endows MNPs with the high structural stability with only a marginal increase in their hydrodynamic diameter [52, 97]. For example, 2,3-dimercaptosuccinic acids (DMSAs) could stabilize 12 nm-sized Fe_3O_4 NPs through chelate bonding of the carboxylate group to the MNPs and structural stabilization by disulfide cross-linkages between the ligands, and the remaining free thiol group of the ligand could be used for further bioconjugation [97]. These results indicated that these DMSA-coated MNPs were fairly stable in the phosphate-buffered saline (PBS) which were sufficiently suitable for in vivo utilization.

The other ligands, including the oligonucleotides, polysaccharides, acids, and amines, are also widely used in the surface modification of MNPs. Take folic acid (FA) for example; Hayashi et al. had designed the MNP nanoclusters modified with FA and PEG to promote their accumulation in tumors [98]. The surface modification was attained simultaneously as follows: (1) several allyl-MNPs became enclosed by PEG via the thiol–ene click reaction with thiol-functionalized PEG (SH-PEG), resulting in forming SH-PEG-MNP nanoclusters, and (2) FA-PEG-MNP nanoclusters were then produced when using thiol- and FA-heterobifunctionalized PEG (SH-PEG-FA) instead of SH-PEG [98]. The clustered FA-PEG-MNPs with high relaxivity and the SAR value were potentially used for the cancer targeted hyperthermia (See Sect. 2.3).

As a whole, the utilization of ligand conjugation can markedly improve colloidal stability of MNPs in aqueous solutions. But the thin ligand coating is not a good enough barrier to prevent oxidation of the highly reactive metal particles, and the ligand-coated MNPs indicate relatively low intrinsic stability in solution at higher temperature and other pH [20]. So the development of other surface modification methods for protecting MNPs against deterioration is of great importance.

2.1.3.2 Hydrophobic Interaction

An alternative approach for noncovalent binding to the MNP surface relies on the hydrophobic interaction. In this method, lipid-based colloidal aggregates, such as liposomes, microemulsions, and micelles, can carry hydrophilic cargo in the aqueous lumen and hydrophobic cargo in the lipid membrane interior [99]. They have been used extensively in recent decades as MNP surface coating and drug carriers to improve pharmacokinetic properties or the bioavailability of the drug, to increase the target-to-background ratio of the drug or MNPs [19, 99–107]. In one method of lipid functionalization of the MNP surface, MNPs and lipids are first coprecipitated and then redispersed in water [19, 100]. In another method, the MNPs and lipids are incorporated together through an emulsion formed by an organic solvent and water, and the excess coating material is removed by magnetic separation [101]. For instance, Anderson's group developed a simple method to coat MNPs with a cationic lipid-like material. Herein, the monodisperse MNPs were first dispersed along with oleic acid and lipids in chloroform. Instead of completely drying the forming emulsions, the solvent *N*-methyl-2-pyrrolidone (NMP) was then added to induce adhesion between the MNP surface and lipids and sonicated under nitrogen protection. Finally, the chloroform was thoroughly evaporated away, which prevented phase separation when particles were transferred to the aqueous phase (Fig. 2.7a) [19]. The lipid-coated magnetic aggregates as delivery platform here were capable of delivering DNA and siRNA to cells, which could offer the potential for magnetically guided targeting, as well as an opportunity to combine gene therapy with MRI and magnetic hyperthermia (See Sects. 2.2 and 2.3).

Another ideal magnetic nanoscale drug delivery lipid vehicle was designed and achieved by stealth liposomes comprising self-assembled superparamagnetic iron oxide NPs individually stabilized with palmityl-nitroDOPA incorporated in the lipid membrane, as was shown in Fig. 2.7b. The ACMF was used to control the timing and dose of repeatedly released thermally sensitive cargo from such lipid vesicles by locally heating the membrane and changing its permeability. This novel delivery system thus created the possibility to assemble and track versatile and efficient drug delivery vehicles and nanoreactors [102].

The PEG–phospholipid has also been used to improve the stability and pharmacokinetics of MNPs in the physiological environment [105–107]. On the one hand, the lipid coating on the MNP surface can provide remarkable biocompatibility and biodegradability, and on the other the PEG polymers located at outmost layers are used extensively for improving blood circulation in vivo. Bao's group developed a new solvent-exchange method, in which PEG–lipid copolymer (DSPE-mPEG) and MNPs assembled in a solvent system with ascending solvent polarity [105]. They found that the assembly of amphiphilic molecules on hydrophobic surface of 14 nm-sized MNPs can be induced controllably by increasing the polarity of solvent systems with miscible solvents. Similarly, Zhang's group synthesized a well-established Mn–Zn ferrite MNPs coated with DSPE-PEG2000 through hydrophobic interaction between lipid and oleic acid/oleylamine (Fig. 2.7c). The monodisperse PEGylated MNPs with core–shell structure (15 nm) exhibited excellent performance, such as high magnetism of 98 $\mathrm{emu \cdot g^{-1}}$ Fe, *r2* of 338 $\mathrm{mM^{-1}s^{-1}}$, and SAR value of 324 $\mathrm{W\ g^{-1}}$ Fe [106]. These advantages endowed them with efficient passive targeting ability in vivo for prominent tumor MRI and magnetically induced heating when exposed to ACMF, based on EPR effects (See Sect. 2.3).

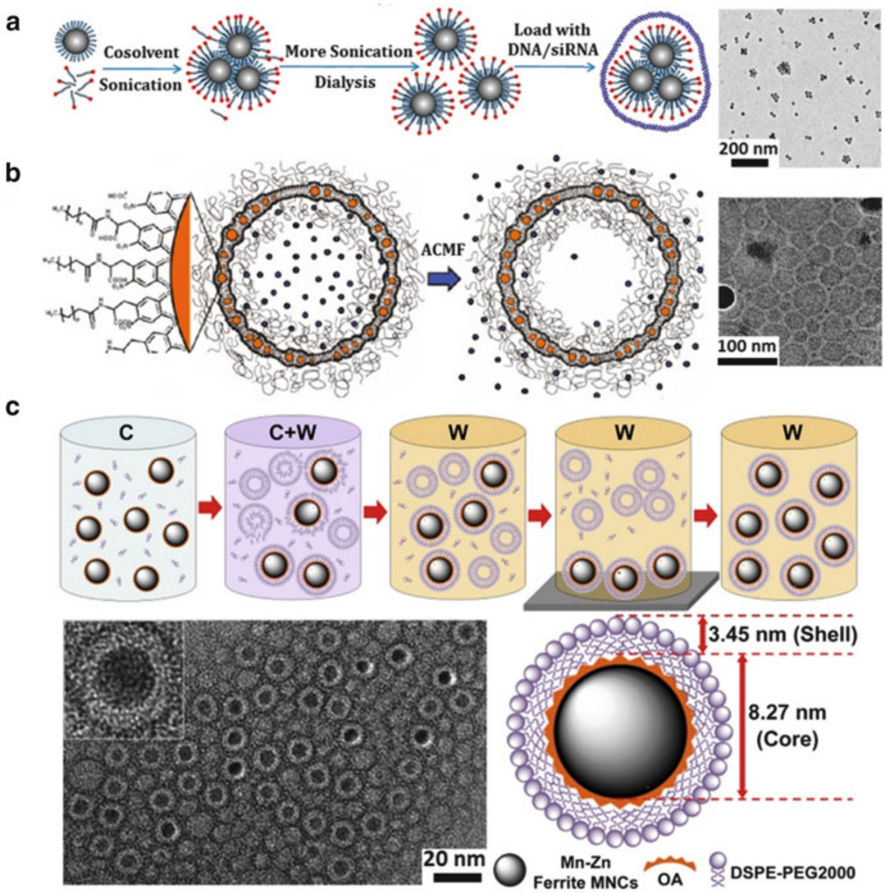

Fig. 2.7 (**a**) Schematic plot of the procedure of lipid-coating iron oxide nanoclusters and corresponding TEM image (Reprinted with permission from Ref. [19]. Copyright 2013, American Chemical Society). (**b**) Schematic of drug-loaded liposomes containing iron oxide NPs in their bilayer and the triggered release under the ACMF (Reprinted with permission from Ref. [102]. Copyright 2011, American Chemical Society). (**c**) A schematic diagram of PEGylated lipid-coated Mn–Zn ferrite MNP synthesis (C, chloroform; W, water) and TEM images/schematic diagram of PEGylated lipid-coated MNPs (Reprinted with permission from Ref. [106]. Copyright 2014, Elsevier)

2.1.3.3 Precious Metal and Inorganic Material Coating

Some precious metals and inorganic materials can be deposited on magnetic nanoparticles through reactions in the chemical conjugation, microemulsion, redox transmetalation, iterative hydroxylamine seeding, or other methods, to protect the cores against oxidation and to improve their functionality [75, 76, 108–113]. In a precious metal coating, the bifunctional composite nanostructure containing Au/Ag and MNPs is traditionally obtained by physical deposition of a thin Au/Ag film onto a spherical MNP, by adsorption of $HAuCl_4$ on the MNP surface followed by the reduction, or via electroplating through the nanoscale templates [75, 76, 108, 109]. For instance, Sun's group reported the dumbbell-like Au–Fe_3O_4 NPs, as illustrated in Fig. 2.8a. They firstly synthesized Au NPs by injecting $HAuCl_4$ solution into the reaction mixture and then in situ decomposing the $Fe(CO)_5$ precursors on the surface of the Au NPs followed by oxidation in 1-octadecene solvent in the presence of oleic acid and oleylamine and heating the mixture to reflux (300 °C), leading to dumbbell-like Au–Fe_3O_4 NPs [108]. Additionally, they also presented a facile synthesis of Au- and Ag-coated Fe_3O_4 NPs with core–shell structure [109]. The synthesis started with room temperature coating of Au on the surface of Fe_3O_4 NPs by reducing $HAuCl_4$ in a chloroform/oleylamine solution. The Au-coated Fe_3O_4 NPs were then transferred into water by mixing them with sodium citrate and cetyltrimethylammonium bromide (CTAB) (Fig. 2.8b). The water-soluble Fe_3O_4/Au NPs served as seeds for the formation of Fe_3O_4/Au NPs with thicker Au coating by simply adding more $HAuCl_4$ in the reducing condition or for the preparation of Fe_3O_4/Au/Ag NPs by adding $AgNO_3$ to the reaction mixture [109]. Wang et al. also developed the monodispersed core–shell Fe_3O_4@Au NPs by chemical deposition (Fig. 2.8c) [76, 110]. Following the formation of Fe_3O_4 NPs as seeds with the desired sizes, Au was deposited onto the surface of Fe_3O_4 NPs by the reduction of $Au(acac)_3$ in the presence of capping and reducing agents at elevated temperature (180 ~ 190 °C) [110]. In this process, the careful manipulation of the reaction temperature was the key factor, which could control the thermally activated deposition of Au on the exposed Fe_3O_4 NP surface and subsequent re-encapsulation of the Au shell surface by the capping agent [76].

The gold coating on the surface of MNPs functionalized with thiol (–SH) or amino (–NH_2) groups as another surface modification method is especially interesting recently, since the gold surface can be easily functionalized with these groups [111, 112]. This treatment allows further linkage of functional ligands which may make the MNPs@Au suitable for catalytic and other optical applications. For instance, Goon et al. reported a facile method of synthesizing 50 ~ 150 nm MNPs@

→

Fig. 2.8 (**a**) Schematic diagram of dumbbell-like Au–Fe_3O_4 NP synthesis and corresponding TEM images (Reprinted with permission from Ref. [108]. Copyright 2005, American Chemical Society). (**b**) Schematic illustration of hydrophilic Fe_3O_4/Au NP synthesis and corresponding TEM images (Reprinted with permission from Ref. [109]. Copyright 2007, American Chemical Society). (**c**) The formation of Fe_3O_4@Au NPs in the presence of capping agents which involves capping-shell desorption, deposition of Au on the exposed Fe_3O_4 surface, and re-encapsulation, TEM images, and size distributions of the Fe_3O_4@Au NPs (Reprinted with permission from Ref. [110]. Copyright 2005, American Chemical Society). (**d**) Schematic representation of the synthesis of Fe_3O_4@Au NPs, based on the PEI self-assembled onto negatively charged Fe_3O_4 NPs and corresponding TEM image (Reprinted with permission from Ref. [111]. Copyright 2009, American Chemical Society). (**e**) Schematic illustration of bifunctional Au–Fe_3O_4 NP synthesis by chemical bond (such as Au–S) interaction and corresponding TEM images (Reprinted with permission from Ref. [112]. Copyright 2007, American Chemical Society)

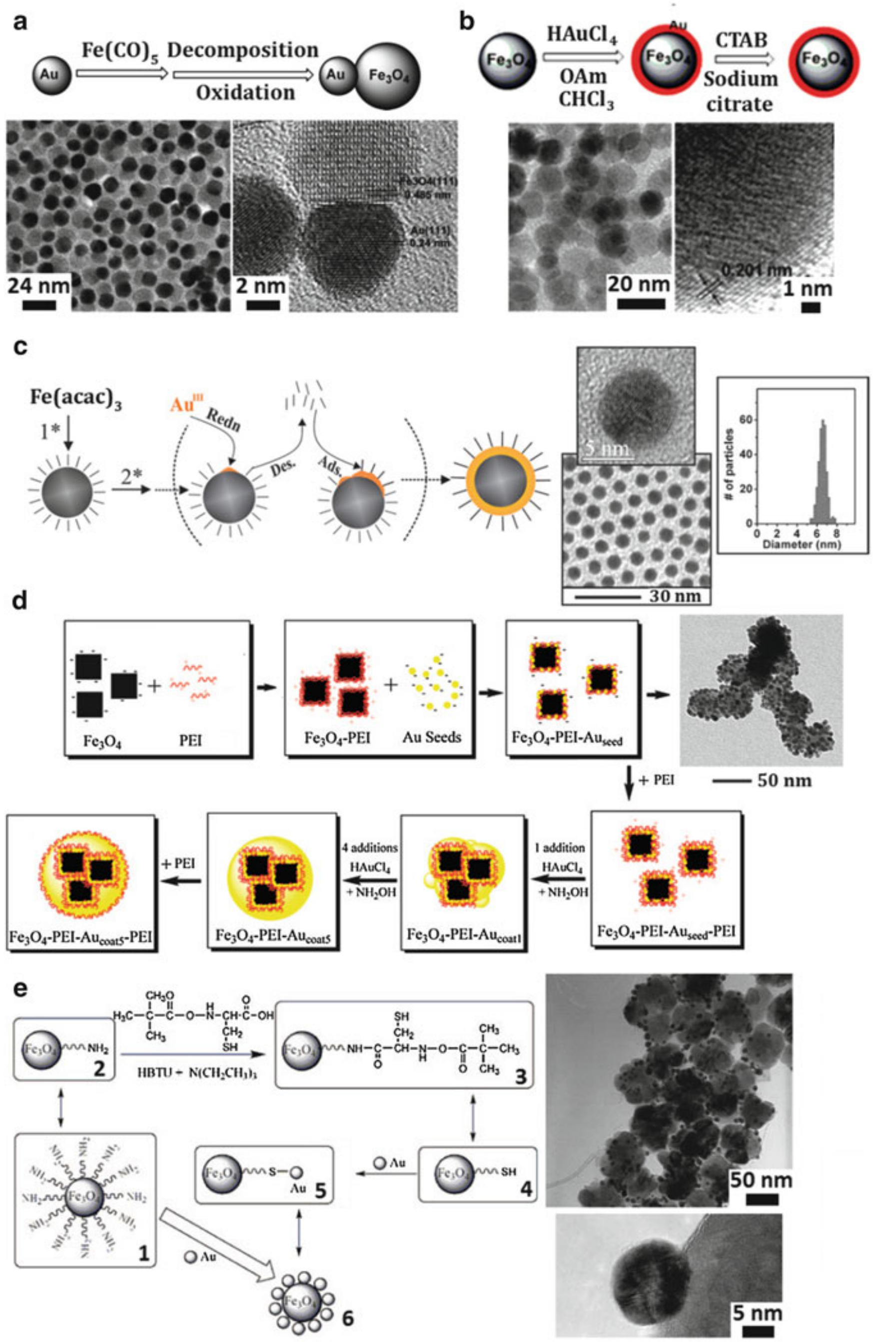
a
Au
Fe(CO)5 Decomposition
Oxidation
Au Fe3O4
Fe3O4(111) 0.485 nm
Au(111) 0.24 nm
24 nm
2 nm
b
Fe3O4
HAuCl4
OAm
CHCl3
Au
CTAB
Sodium citrate
0.201 nm
20 nm
1 nm
c
Fe(acac)3
1*
2*
AuIII
Redn
Des.
Ads.
5 nm
30 nm
# of particles
Diameter (nm)
d
Fe3O4
PEI
Fe3O4-PEI
Au Seeds
Fe3O4-PEI-Auseed
+ PEI
50 nm
Fe3O4-PEI-Auseed-PEI
1 addition
HAuCl4
+ NH2OH
Fe3O4-PEI-Aucoat1
4 additions
Fe3O4-PEI-Aucoat5
Fe3O4-PEI-Aucoat5-PEI
e
HBTU + N(CH2CH3)3
Fe3O4
NH2
SH
Au
1
2
3
4
5
6
50 nm
5 nm

Au composites via the use of a biocompatible polyethyleneimine (PEI) for the dual function of attaching gold seeds and preventing the formation of large aggregates [111]. They showed that successful Au coating of MNPs requires the self-assembly of a layer of PEI onto MNP cores by Au–N chemical bond interaction and subsequent saturation of the surface with 2 nm gold seeds. In order to form a protective layer of gold shell, the additional PEI could be used to increase MNPs@Au stability against aggregation, which was important for further application (Fig. 2.8d) [111]. Bao et al. had reported their recent success in the synthesis of bifunctional Au–Fe_3O_4 NPs that are formed by simply linking two separately prepared nanomaterials by chemical bond (such as Au–S) interaction, rather than using chemical deposition processes (Fig. 2.8e) [112]. Due to the introduction of Au nanoparticles, the resulting bifunctional Au–Fe_3O_4 NPs could be easily modified with other functional molecules to realize various technological separations and detections simply under a magnet [112].

Except for the precious metal coating, of some inorganic materials, such as silica, carbon coatings also have the advantages arising from the higher chemical and thermal stability as well as biocompatibility and easy surface modification [20, 113–118]. A silica shell does not only protect the magnetic cores but also prevent the direct contact of the magnetic core with additional agents linked to the silica surface, thus avoiding unwanted interactions [20]. Xia et al. had shown that the commercially available MNPs can be directly coated with silica shells by the hydrolysis of tetraethoxysilane (TEOS) [113]. The MNPs here were diluted with deionized water and 2-propanol, and then ammonia solution and various amounts of TEOS were added to the reaction mixture under stirring at room temperature for about 3 h. The coating thickness could be controlled by changing the amount of TEOS [113]. Johnson et al. had described a simple method to prepare carbon-coated magnetic Fe and Fe_3C NPs by direct thermal decomposition of the iron stearate at 900 °C under an argon atmosphere [117]. Lu et al. had synthesized highly stable 11 nm-sized carbon-coated cobalt MNPs. They indicated that the cobalt NPs could be coated with furfuryl alcohol which was converted first into poly(furfuryl alcohol) and then carbonized in the presence of CTAB used as the carbon source during the pyrolysis, resulting in a stable protection layer against air oxidation [118].

2.2 MNPs with High Performance for MR Imaging Diagnostics

Recently, biomedical imaging techniques including representative positron-emission tomography (PET), magnetic resonance imaging (MRI), and X-ray computed tomography (CT) are vital in the diagnosis of various diseases due to their analytic ability at molecular or cellular levels [7, 8, 10, 52, 119–123]. In this regard, a new discipline, known as “molecular imaging,” which combines molecular biology and in vivo imaging, has emerged. MRI as one of the most powerful diagnosis techniques has been the preferred tool for the brain and the central nervous system imaging and for the tumor detection, since it can give noninvasive, highly sensitive, and target-specific detection of diseases by the help of MRI contrast agents. In general, the MRI contrast agents should possess as high as possible relaxivity and as small as possible size. In the past years, a variety of MNPs, such as superparamagnetic iron oxide nanoparticles, are important and representative MRI contrast agents, and it has received great attention for clinical liver imaging [124, 125]. These MNP-based MRI contrast agents are composed of three parts: (1) the magnetic core, which can generate distinct MR signal enhancement; (2) the surface water-dispersible layers of MNPs, which endow their compatibility and stability in the biological environment; and (3) the bioactive materials on the terminal of MNPs for their active targeting purpose [124].

Under an applied magnetic field (B_0), the designed MNPs are magnetized with additional magnetic moment and generate an induced magnetic field, perturbing the nuclear spin relaxation processes of the water protons. Based on their relaxation processes, some conventional MRI contrast agents are mostly effective in a single imaging mode of either longitudinal (*T1*) relaxation mode (bright signals) or transverse (*T2*) relaxation mode (dark signals) (Fig. 2.9a) [8]. The commercially available *T1* contrast agents are usually paramagnetic complexes, while *T2* contrast agents are based on iron oxide nanoparticles. Take the typical *T2*-MR contrast effect for example; the magnetic relaxation processes of the water protons in the presence of MNPs are perturbed, and the spin–spin relaxation time is shortened. The perturbation leads to the MR signal contrast enhancement, which appears as a darkening of the corresponding MR image [52] (Fig. 2.9b). The degree of the *T2* contrast effect is represented by the spin–spin relaxivity $R2$ ($R2 = 1/T2$), and the relaxivity

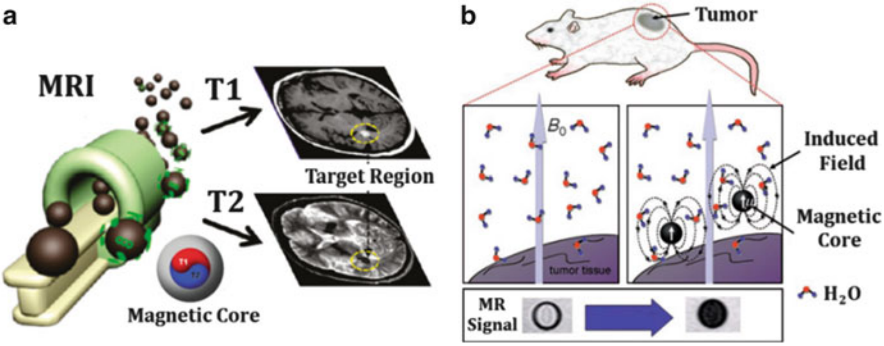

Fig. 2.9 (**a**) Responsive MR signals for a bright image in the T1 mode and a dark image in the T2 mode (Reprinted with permission from Ref. [8]. Copyright 2011, American Chemical Society). (**b**) MR contrast effects of MNPs. Under an external field (B_0), the MNPs are magnetized with a magnetic moment and generate an induced magnetic field which perturbs the nuclear spin relaxation processes of the water protons. This perturbation leads to MR contrast enhancement which appears as darkening of the corresponding section of the MR image (Reprinted with permission from Ref. [52]. Copyright 2008, John Wiley & Sons Ltd)

coefficient ($r2$), which is obtained as the gradient of the plot of $R2$ versus the molarity of magnetic atoms, is a standardized contrast-enhancement indicator [52].

The MR contrast-enhancement effect in vivo of MNPs can be greatly influenced by their size, shape, magnetism, surface chemistry, and biocompatibility, which are the most important considerations in clinical cancer early detection and diagnosis. Therefore, the development of the MNPs with high performance is particularly important. In recent years, some relevant research groups have developed a variety of MNPs with excellent magnetic properties, high sensitivity, low toxicity, long blood circulation, and specific target function served as contrast-enhancing MRI probes. We can attempt from the following cases [105, 126–128]. For instance, Tong et al. have described a method for coating magnetic iron oxide nanoparticles with phospholipid PEG1000 through the hydrophobic interaction between lipid and oleic acid/oleylamine on MNP surface. They further demonstrate that, by fine-tuning the core size and PEG coating of MNPs, the $r2$ relaxivity per particle can be increased by >200-fold. With 14 nm core and PEG1000 coating, the MNPs have $r2$ relaxivity of 385 $\mathrm{mM^{-1}s^{-1}}$, which is among the highest per-Fe atom relaxivities. In addition, intravenous injection of the MNPs resulted in the significant enhancement in $T2$-MRI contrast of tumor tissue, which demonstrated the potential of the MNPs for clinical applications (Fig. 2.10a) [105]. In addition, Lee et al. have developed a new $MnFe_2O_4$–Herceptin probe with high performance to make the ultrasensitive in vitro detection of cancer cells possible since the probe interacts with all HER2/neu-positive cancer cells. Significantly, improved $T2$-MR imaging of cancers is possible utilizing this probe which has a large $r2$ of 358 $\mathrm{mM^{-1}s^{-1}}$. When the MNP probe is tail intravenously injected into a mouse, very small tumors can be specifically detected with a high MR contrast effect. In particular, these MNPs with high performance have little toxicity for potential in vivo ultrasensitive cancer imaging applications. These features make them appealing candidates for early detection and diagnosis of cancer and many other diseases (Fig. 2.10b) [10, 52, 121].

2.3 MNPs with High Performance for Cancer Targeted Hyperthermia

Magnetically induced heat generation from NPs can be used for various purposes including cancer therapy known as hyperthermia [7, 8, 129–138]. Once the MNPs are in the desired location in vivo (where they are concentrated) upon exposure to an ACMF with appropriate field and frequency, the MNPs continuously emit heat via Néel and Brownian pathways (Fig. 2.11a), generating heat and increasing the temperature of the surrounding diseased tissue. Ideally, the cancer tissue is heated to approximately 42 ~ 55 °C, which reduces the viability of the cancer cells. Comparing with the conventional radio frequency-, microwave-, and laser wavelength-induced thermotherapy, the magnetic hyperthermia is more superior and predominant. It can focus on the MNPs' exact location of both transplantable

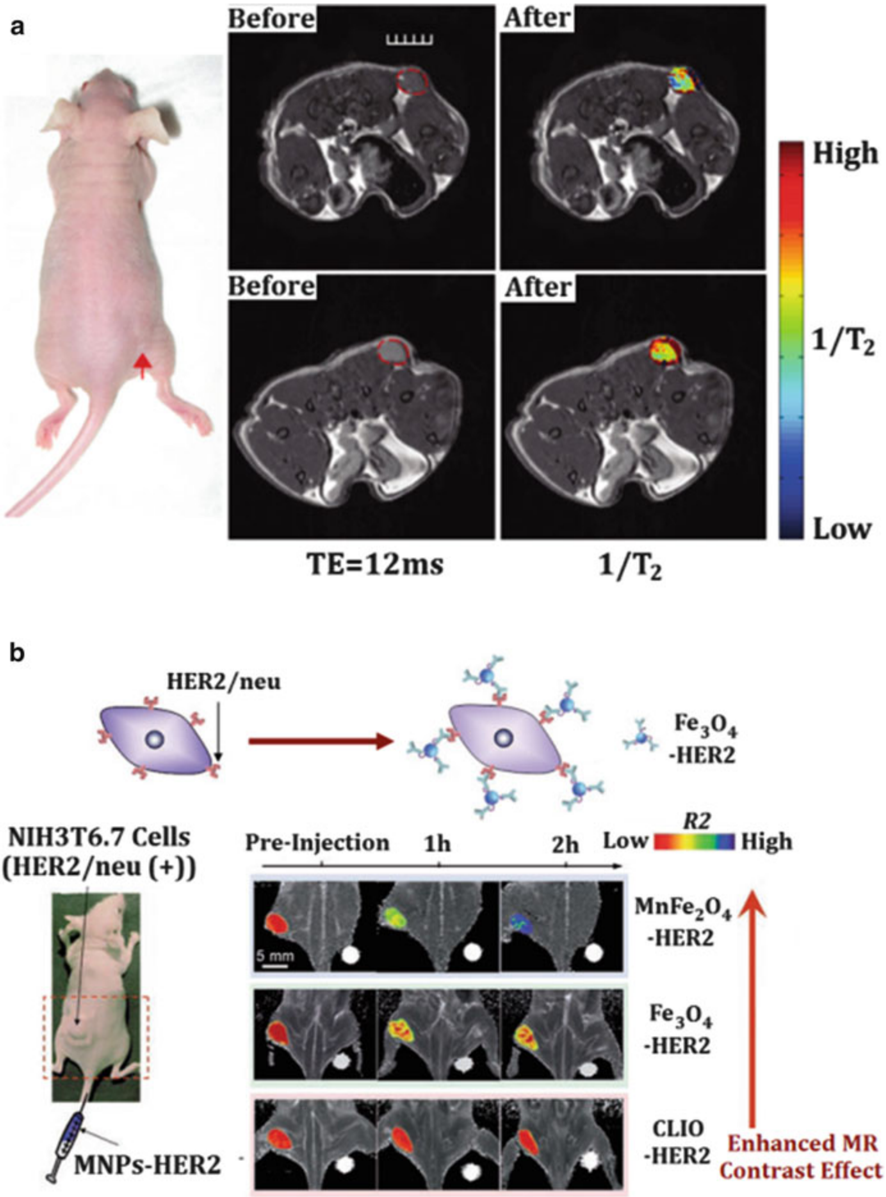

Fig. 2.10 (**a**) In vivo tumor MR imaging. *Arrow* shows the location of the subcutaneous tumor and MR images of tumor before probe injection. MR images collected after 1 h following the injection of 14 nm MNPs conjugated with antibodies against mouse VEGFR-1 (Reprinted with permission from Ref. [105]. Copyright 2010, American Chemical Society). (**b**) Intravenous tail vein injection of the MNP–Herceptin probes into a mouse with a small HER2/neu-positive cancer in the proximal femur region. In comparison, MNP–Herceptin probes and CLIO–Herceptin probes were also tested. Color-mapped MR images of the mouse at different times following injection (Reprinted with permission from Ref. [10]. Copyright 2007, Macmillan Publishers Ltd, Ref. [52]. Copyright 2008, John Wiley & Sons Ltd, and Ref. [121]. Copyright 2005, American Chemical Society)

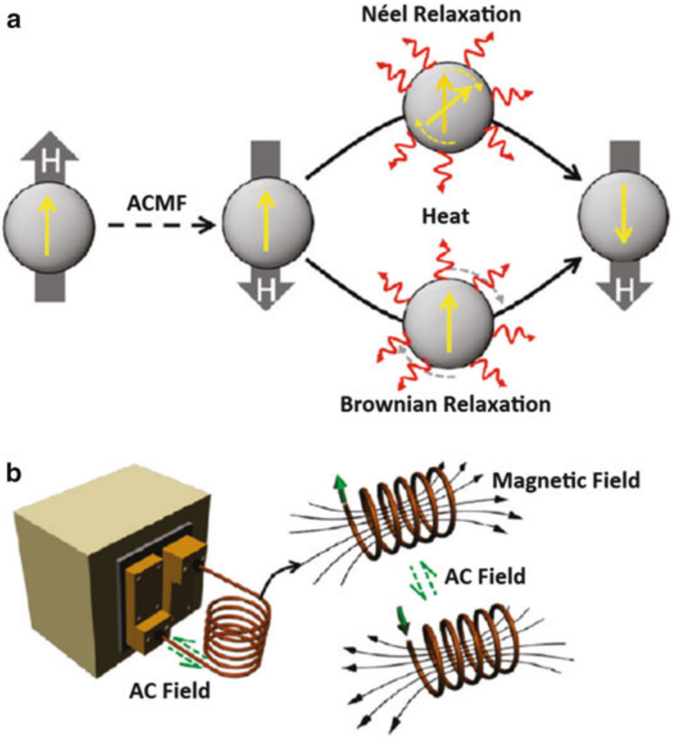

Fig. 2.11 The MNPs for magnetic hyperthermia under an ACMF: (**a**) Néel and Brownian relaxation processes and (**b**) experimental apparatus (Reprinted with permission from Ref. [8]. Copyright 2011, American Chemical Society)

and in situ carcinoma in vivo and provides a noninvasive way to efficiently raise the tumor temperatures to therapeutic levels [8, 133], which is considered a promising cancer therapy in further clinical application.

The magnetic hyperthermia device consists of the radio link control (RLC) circuit, including the resistor, inductor, and capacitor, causing the induction of an ACMF. The water-jacketed coil is usually used to cool down the coil temperature (Fig. 2.11b) [8]. Unfortunately, most of the studies on magnetic hyperthermia used harmful ACMF with high amplitude and frequency for patients in clinical application. Some experiments have shown that the designed low- or mid-frequency ACMF (100 ~ 400 kHz) has been demonstrated to be safe and beneficial for potential application [7, 8, 134, 135], and data on the therapeutic effect of the hyperthermia assessed under ACMF with the product of the amplitude and frequency of $<5 \times 10^9$ $\mathrm{Am^{-1}s^{-1}}$ is required [136–138], but to date, none of the FDA-approved MNPs have been exploited for hyperthermia purposes. The first instance of selective inductive heating of lymph nodes using MNPs under an ACMF was probably in 1957 [139], since then the MNP-mediated hyperthermia in vivo has progressed much. But the clinical trial of MNPs designed by Jordan et al. for hyperthermia had been at Berlin's Charité Hospital in 14 patients with a severe type of brain cancer using local injection of 15 nm-sized iron oxide NPs in a water suspension. The field amplitudes here between 3.8 and 13.5 kA m^{-1} at 100 kHz were employed [140]. Johannsen et al. also had used an ACMF with a frequency of 100 kHz and variable field strength of 0 ~ 18 kA m^{-1} in clinical use. To measure heating rate in situ, fiber-optic thermocouples were surgically positioned into the prostate, urethra, rectum, perineum, scrotum, and left ear and monitored with software to keep field strength constant or be adjusted to the desired temperatures [141]. In addition, the favorable recent results of "nanothermotherapy" study in clinical phase II led by German company MagForce Nanotechnologies [130–132] demonstrated the magnetic hyperthermia potential.

In the majority of cases, the MNP-mediated cancer hyperthermia therapy strategies are applied in two ways: (1) the high temperature for short-time periods (>50 °C for 10 ~ 30 min) in tumor tissue, commonly referred to as thermal ablation, and (2) the lower temperatures for long-time periods (42 ~ 45 °C for at least 30 min) in tumor tissue often called mild hyperthermia [142]. Generally, the threshold thermal exposure for mild hyperthermia treatment can induce distinct apoptosis effect. Simultaneously, it can result in the tumor vascular damage and the reduction in tumor blood flow in the vasculature, thereby impairing oxygen and nutrient supply, inducing the anti-angiogenesis effect [106]. Whereas thermal ablation can alter the tumor microenvironment in terms of hypoxia, perfusion in tumors and immunological function kill the tumor cells directly with heat treatment and finally lead to tumor tissue necrosis and coagulation [7]. The heat ablation induction can also raise the metabolism and transition (meaning the structural transformation from an ordered to a disordered state) of cellular structures, such as DNA and proteins [7, 142–144]. Accordingly, protein aggregation, insolubilization, increased fluidity of cellular membranes, disruption in ion permeability through cellular membranes, inhibition of amino acid transport, morphological changes as a consequence of damaged cytoskeletal system, and inhibition of DNA repair are typical effects at the cellular level [7, 142]. For instance, in an experiment conducted by Hilger et al., the tumor-bearing mice received an intratumoral injection of iron oxide NPs at 4–18 mg per 100 mg tumor tissue and were then exposed to an ACMF (amplitude, 6.5 kA m^{-1}; frequency, 400 kHz) for 50 min. During hyperthermia treatment, the temperature of tumor tissue changes varied from 12 °C to 73 °C, and the histological examination of the tumor tissue revealed the presence of the early stages of coagulation and necrosis [145]. Huang et al. had described the use of the MNPs that, with a well-tolerated intravenous dose, achieved a tumor concentration of 1.9 mg [Fe]/g tumor in a subcutaneous carcinoma mouse model. With an ACMF of 38 kA m^{-1} at 980 kHz, tumor tissue could be heated to 60 °C in 2 min, durably ablating them with millimeter precision, leaving the surrounding tissue intact [146]. More recent studies have also focused on increasing the efficiency of this thermal ablation treatment [147–149]. Although thermal ablation can effectively destroy tumor tissue, a major limitation with this type of therapy in its overall effectiveness is due to the difficulties of heating large tumors. In this regard, designing an effective magnetic hyperthermia strategy, such as the MNP injection method and dose, and the appropriate size of ACMF helical coil device, to make sure the whole tumor tissue region reaches a sufficient temperature, is challenging for researchers.

Direct intratumoral injection of MNPs is a conventional method for magnetic hyperthermia, which is demonstrated to be safe and beneficial in clinical application [146, 147]. It has the advantages of achieving high concentrations of MNPs in the tumor regions and inducing tumor thermal ablation under the exposure to ACMF, rapidly controlling tumor growth. But it severely suffers from not covering tumors adequately, being invasive, and typically leaving undertreated regions, leading to the cancer regrowth [146]. In contrast, intravenous administration of MNPs covers irregular tumor shapes more precisely, loads many tumors simultaneously, and is minimally invasive, which has a practical advantage in cancer targeted magnetic hyperthermia (TMH) [106]. Previous attempts to implement intravenous injection of MNPs followed by ACMF heating showed some efficacy but were not able to fully ablate tumors, as required concentration was not reached in the tumors [150, 151]. Additional barrier to this approach was the toxicity of the MNPs at a level that achieves the required tumor loading after injection.

To achieve adequate concentrations of MNPs in the tumor, the excellent performances of MNPs, such as the higher magnetic characteristic, biocompatibility, and increased tumor-targeting ability, are crucial for their successful cancer TMH. As previously mentioned, one way of characterizing the heating ability of MNPs under an ACMF is calculating their SAR values. Firstly, there is a great challenge for optimizing the size, shape, and structure of MNPs to achieve higher heating power. In detail, it was shown that the spherical MNPs with a mean size of ~20 nm are suitable for clinical hyperthermia as the previous depiction [152], and cubic-shaped iron oxide NPs or flower-shaped NPs had recently shown considerably improved hyperthermia properties, compared to optimized 20 nm spherical iron oxide NPs [72, 137]. The current progress in the synthesis of MNPs now allowed for their variable and controlled core–shell structures [80]. A very important antitumor effect induced by hyperthermia had been thus noticed with core–shell MNPs consisting of a core displaying a high magnetic anisotropy surrounded by a shell with a small magnetic anisotropy [80]. In an attempt to develop new ferrite NPs with higher thermal energy transfer capability, a metal-dopant (e.g., Mn^{2+} or Zn^{2+}) substitution strategy had also been pursued in recent studies [52, 78]. For instance, it was proved that this strategy for enhancing SAR value (432 W g^{-1}) of doped $(Zn_{0.4}Mn_{0.6})Fe_2O_4$ NPs, achieving higher nanomagnetism, was very important. The high SAR could bring better efficacy with lower dosage levels, leading to a fourfold enhancement in hyperthermic effects in vitro compared to conventional Feridex measured under an ACMF at 500 kHz and 37 kA m^{-1} [78]. In the study of Zhang et al., doping Mn–Zn ferrite MNPs (8 nm) were proved to exhibit extremely high magnetization value with 98 emu g^{-1} Fe and a magnetically induced temperature elevation (~30 °C in aqueous solution for 15 min by application of an ACMF with 390 kHz and 12 A) [106]. The outstanding performances made the MNPs promising as an excellent material for early diagnosis and therapy in vivo.

Secondly, the improved MNP-mediated tumor-targeting efficiency as another strategy plays a vital role in practical TMH in vivo. As an essential challenge, the

MNPs should be conjugated to the surface coating or targeting molecule to achieve efficient accumulation in tumor tissues with MNP-mediated intravenous injections. Generally, the leaky vasculature of tumors may promote MNP accumulation as the blood flows through the tumor, but the MNPs without surface modification are rapidly cleared from the blood circulation when passing through the biological defense system and vascular barriers in vivo [129]. When the immune system does not recognize the MNPs, the MNPs may have a longer blood circulation time, promoting their passive targeting ability and increasing their accumulation in the tumor tissue because of the aforementioned EPR effect. The previously mentioned coatings (e.g., specifically PEG and liposomes) are the mostly responsible for passive targeting effect and increased blood circulation time of the MNPs. It was proved that the lipid DSPE-PEG2000-coated Mn–Zn ferrite MNPs with a core–shell structure in an average diameter of 48.6 nm can drastically minimize the recognition and phagocytosis of macrophages and simultaneously improve their biocompatibility, which endowed them with efficient passive targeting ability in vivo for prominent magnetically induced heating when exposed to ACMF, based on the EPR effects (Fig. 2.12a) [80, 106]. To ensure sufficient accumulation, the use of MNPs with a well-tolerated intravenous single dose of 18 mg Fe kg^{-1} mouse body weight was described. With an ACMF of 12 A at 390 kHz, the tumor surface sites could be heated to approximately 43 °C in 30 min based on MNC-mediated intravenous injections [106]. The MNP-mediated passive targeting can successfully accumulate at tumors, but there is also concurrent accumulation in some other tissues, most notably the liver and spleen. It makes the restricted use of passive targeting for tumor hyperthermia purpose.

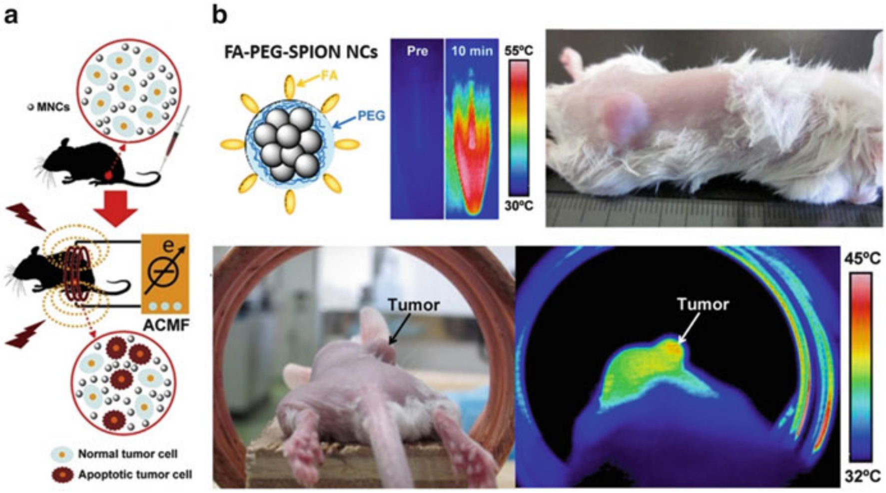

Fig. 2.12 (**a**) A schematic diagram of MNPs for the magnetically induced mice cancer theranostics (Reprinted with permission from Ref. [106]. Copyright 2014, Elsevier). (**b**) The FA-PEG-SPION NPs with intravenous administration for mice cancer TMH (Reprinted with permission from Ref. [98]. Copyright 2013, Theranostics)

Approaches of MNP-mediated active targeting in relation to TMH are proposed with the aim of improving the MNP accumulation beyond passive targeting. It has the advantage that MNPs can be selectively deposited in the tumor region after the intravenous application without needing to puncture the tumor tissue with intratumoral injection methods. The active targeting ligands, such as antibodies, tat peptides, RGD peptides, FA, and chlorotoxin, are often modified on the initial surface of MNPs [129]. The targeting ligands can increase the cellular uptake of MNPs in targeted cell either by endocytosis or binding to targeted cell surface. A promising active targeted hyperthermia method for treating prostate cancer was developed by Cui et al., in which they synthesized fluorescent MNPs conjugated with single-chain Fv antibody against an overexpressed γ-seminoprotein [153]. Through studies of targeted MNPs intravenously administered into mice, they showed a steady increase of MNP concentration in the tumor after 2, 6, 9, 12, and 24 h injection. Mice receiving treatment with a magnetic field had a longer life expectancy (7 weeks) than mice not receiving treatment with a magnetic field (4 weeks) [129, 153]. Hayashi et al. had also modified the magnetic nanoclusters with FA, to promote sufficient accumulation in tumors [98]. Twenty-four hours after intravenous injection of FA-modified nanoclusters, they accumulated locally in the cancer tissues. The tumors of the mice then underwent local heating by application of an ACMF (8 kA m^{-1} and 230 kHz) for 20 min. The temperature of the tumor was higher than the surrounding tissues by ~6 °C (Fig. 2.12b) [98].

Thirdly, for clinically available TMH, the optimization of ACMF with adequate frequency, field, and helical coil device is also challenging, which can provide the base for theranostics strategies. It was used in the MNP-mediated hyperthermia clinical trial treating prostate cancer using a 100 kHz machine designed for human patients and later in human glioma trials which demonstrated to be safe and have some benefits [140, 141]. In the experiments of mice modes, the highest amplitude and frequency of an ACMF were set to 38 kA m^{-1} and 980 kHz, in which the mice were observed to have no obvious clinical signs of toxicity (no weight loss or abnormal behavior) [146]. Xie et al. designed a magnetic induction coil device with 3 cm in diameter and 1.5 cm in length in ACMF. The designed ACMF system just made the tumor region of a mouse placed in the center of magnetic induction, focusing the heat into very small tumor regions, and promoted higher thermal energy production, which was used for making TMH a more effective approach to cancer therapy with decreased risk of heating surrounding healthy tissues (e.g., liver and spleen) [106].

The TMH has recently emerged as a promising therapeutic approach for cancer treatment due to intravenous administration of MNPs with high performance to deliver a therapeutic dose of heat specifically to cancerous regions under ACMF. However, it is proved that the single injection of MNPs was difficult in achieving necessary concentration in tumor because of the metabolism and clearance by correlative organs. So the extraordinary strategies of high-quality MNP-mediated TMH attained in further study may be attributed to a combination of the following factors: (1) the dosages of MNCs used here which are considerably larger than that used in previous MR imaging, (2) designing the TMH strategy of repetitious MNP-administered intravenous injections (3 ~ 6 time) and the long-lasting hyperthermia, and (3) the TMH which can combine with other thermotherapies or chemotherapies, triggering the cancer synergetic therapy.

References

1. Li YP, Lin TY, Luo Y et al (2014) A smart and versatile theranostic nanomedicine platform based on nanoporphyrin. Nat Commun 5(4712):1–15
2. Lee DE, Koo H, Sun IC et al (2012) Multifunctional nanoparticles for multimodal imaging and theragnosis. Chem Soc Rev 41:2656–2672
3. Xie J, Lee S, Che XY (2010) Nanoparticle-based theranostic agents. Adv Drug Deliv Rev 62:1064–1079
4. Choi KY, Liu G, Lee S et al (2012) Theranostic nanoplatforms for simultaneous cancer imaging and therapy: current approaches and future perspectives. Nanoscale 4:330–342
5. Luk BT, Fang RH, Zhang LF (2012) Lipid and polymer-based nanostructures for cancer theranostics. Theranostics 2:1117–1126
6. Pan D (2013) Theranostic nanomedicine with functional nanoarchitecture. Mol Pharm 10:781–782
7. Hilger I, Kaiser WA (2012) Iron oxide-based nanostructures for MRI and magnetic hyperthermia. Nanomedicine 7:1443–1459
8. Yoo D, Lee JH, Shin TH et al (2011) Theranostic magnetic nanoparticles. Acc Chem Res 44:863–874
9. Pankhurst QA, Connolly J, Jones SK et al (2003) Applications of magnetic nanoparticles in biomedicine. J Phys D Appl Phys 36:167–181
10. Lee JH, Huh YM, Jun YW et al (2007) Artificially engineered magnetic nanoparticles for ultra-sensitive molecular imaging. Nat Med 13:95–99
11. Rosensweig RE (2002) Heating magnetic fluid with alternating magnetic field. J Magn Magn Mater 252:370–374
12. Gupta AK, Gupta M (2005) Synthesis and surface engineering of iron oxide nanoparticles for biomedical applications. Biomaterials 26:3995–4021
13. Mornet S, Vasseur S, Grasset F et al (2006) Magnetic nanoparticle design for medical applications. Prog Solid State Chem 34:237–247
14. Berkowit AE, Schuele WJ, Flanders PJ (1968) Influence of crystallite size on the magnetic properties of acicular γ-Fe_2O_3 particles. J Appl Phys 38:1261–1263
15. Leslie-Pelecky DL (1996) Magnetic properties of nanostructured materials. Chem Mater 8:1770–1783
16. Xu C, Xu K, Gu H et al (2004) Dopamine as a robust anchor to immobilize functional molecules on the iron oxide shell of magnetic nanoparticles. J Am Chem Soc 126:9938–9939
17. Basiruddin SK, Arindam S, Jana NR et al (2010) Advances in coating chemistry in deriving soluble functional nanoparticle. J Phys Chem C 114:11009–11017
18. Liu SJ, Han YC, Gao MY et al (2010) Investigations on the interactions between plasma proteins and magnetic iron oxide nanoparticles with different surface modifications. J Phys Chem C 114:21270–21276
19. Jiang S, Eltoukhy AA, Love KT et al (2013) Lipidoid-coated iron oxide nanoparticles for efficient DNA and siRNA delivery. Nano Lett 13:1059–1064
20. Lu AH, Salabas EL, Schuth F (2007) Magnetic nanoparticles: synthesis, protection, functionalization, and application. Angew Chem Int Ed 46:1222–1244
21. Neveu S, Bee A, Robineau M et al (2002) Size-selective chemical synthesis of tartrate stabilized. J Colloid Interf Sci 255:293–298
22. Grasset F, Labhsetwar N, Li D (2002) Synthesis and magnetic characterization of zinc ferrite nanoparticles with different environments: powder, colloidal solution, and zinc ferrite-silica core-shell nanoparticles. Langmuir 18:8209–8216

23. Sun SH, Zeng H (2002) Size-controlled synthesis of magnetite nanoparticles. J Am Chem Soc 124:8204–8205
24. Liang HF, Wang ZC (2010) Adsorption of bovine serum albumin on functionalized silica-coated magnetic $MnFe_2O_4$ nanoparticles. Mater Chem Phys 124:964–969
25. Kim DH, Nikles DE, Brazel CS (2010) Synthesis and characterization of multifunctional chitosan-$MnFe_2O_4$ nanoparticles for magnetic hyperthermia and drug delivery. Materials 3:4051–4065
26. Beji Z, Hanini A, Smiri LS et al (2010) Magnetic properties of Zn-substituted $MnFe_2O_4$ nanoparticles synthesized in polyol as potential heating agents for hyperthermia. Evaluation of their toxicity on endothelial cells. Chem Mater 22:5420–5429
27. Robinson DB, Persson HHJ, Zeng H et al (2005) DNA-functionalized MFe_2O_4 (M = Fe, Co, or Mn) nanoparticles and their hybridization to DNA-functionalized surfaces. Langmuir 21:3096–3103
28. Seo WS, Lee JH, Sun XM et al (2006) FeCo/graphitic-shell nanocrystals as advanced magnetic-resonance-imaging and near-infrared agents. Nat Mater 5:971–976
29. Shevchenko EV, Talapin DV, Rogach AL (2002) Colloidal synthesis and self-assembly of $CoPt_3$ nanocrystals. J Am Chem Soc 124:11480–11485
30. Sun SH (2006) Recent advances in chemical synthesis, self-assembly, and applications of FePt nanoparticles. Adv Mater 18:393–403
31. Park J II, Cheon J (2001) Synthesis of “solid solution” and “core-shell” type cobalt-platinum magnetic nanoparticles via transmetalation reactions. J Am Chem Soc 123:5743–5746
32. Kang YS, Risbud S, Rabolt JF et al (1996) Synthesis and characterization of nanometer-size Fe_3O_4 and γ-Fe_2O_3 particles. Chem Mater 8:2209–2211
33. Hong CY, Jang IJ, Horng HE et al (1997) Ordered structures in Fe_3O_4 kerosene-based ferrofluids. J Appl Phys 81:4275–4277
34. Fried T, Shemer G, Markovich G et al (2001) Ordered two-dimensional arrays of Ferrite nanoparticles. Adv Mater 13:1158–1161
35. Zhang ZJ, Wang ZL, Chakoumakos BC (1998) Temperature dependence of cation distribution and oxidation state in magnetic Mn-Fe Ferrite nanocrystals. J Am Chem Soc 120:800–1804
36. Park J, An K, Hwang Y et al (2004) Ultra-large-scale syntheses of monodisperse nanocrystals. Nat Mater 3:891–895
37. Sun SH, Zeng H, Robinson DB (2003) Monodisperse MFe_2O_4 (M = Fe, Co, Mn) nanoparticles. J Am Chem Soc 126:273–279
38. Redl FX, Black CT, Papaefthymiou GC (2004) Magnetic, electronic, and structural characterization of nonstoichiometric iron oxides at the nanoscale. J Am Chem Soc 126:14583–14599
39. Langevin D (1992) Micelles and microemulsions. Annu Rev Phys Chem 43:341–346
40. Wang X, Zhuang J, Peng Q (2005) A general strategy for nanocrystal synthesis. Nature 437:121–124
41. Deng H, Li XL, Peng Q et al (2005) Monodisperse magnetic single-crystal Ferrite microspheres. Angew Chem Int Ed 117:2842–2845
42. Deng H, Li XL, Peng Q et al (2005) Monodisperse magnetic single-crystal Ferrite microspheres. Angew Chem Int Ed 44:2782–2785
43. Cheon J, Kang NJ, Lee SM et al (2004) Shape evolution of single-crystalline iron oxide nanocrystals. J Am Chem Soc 126:1950–1951
44. Ho CH, Tsai CP, Chung CC et al (2011) Shape-controlled growth and shape-dependent cation site occupancy of monodisperse Fe_3O_4 nanoparticles. Chem Mater 23:1753–1760
45. Gao GH, Liu XH, Shi RR (2010) Shape-controlled synthesis and magnetic properties of monodisperse Fe_3O_4 nanocubes. Cryst Growth Des 10:2888–2894
46. Rockenberger J, Scher EC, Alivisatos AP (1999) A new nonhydrolytic single-precursor approach to surfactant-capped nanocrystals of transition metal oxides. J Am Chem Soc 121:11595–11596

47. Farrell D, Majetich SA, Wilcoxon JP (2003) Preparation and characterization of monodisperse Fe nanoparticles. J Phys Chem B 107:11022–11030
48. Jana NR, Chen YF, Peng XG (2004) Size- and shape-controlled magnetic (Cr, Mn, Fe, Co, Ni) oxide nanocrystals via a simple and general approach. Chem Mater 16:3931–3935
49. Samia ACS, Hyzer K, Schlueter JA et al (2005) Ligand effect on the growth and the digestion of Co nanocrystals. J Am Chem Soc 127:4126–4127
50. Li Y, Afzaal M, O'Brien P (2006) The synthesis of amine-capped magnetic (Fe, Mn, Co, Ni) oxide nanocrystals and their surface modification for aqueous dispersibility. J Mater Chem 16:2175–2180
51. Murray CB, Kagan CR (2000) Synthesis and characterization of monodisperse nanocrystals and close-packed nanocrystal assemblies. Ann Rev Mater Sci 30:545–610
52. Jun YW, Lee JH, Cheon J (2008) Chemical design of nanoparticle probes for high-performance magnetic resonance imaging. Angew Chem Int Ed 47:122–5135
53. Vestal CR, Zhang ZJ (2003) Effects of surface coordination chemistry on the magnetic properties of $MnFe_2O_4$ spinel Ferrite nanoparticles. J Am Chem Soc 125:9828–9833
54. Gradmann UJ (1991) Surface magnetism. Magn Magn Mater 100:481–496
55. Kodama RH, Berkowitz AE, McNiff EJ Jr et al (1997) Surface spin disorder in ferrite nanoparticles. J Appl Phys 81:5552–5557
56. Spada FE, Parker FT, Nakakura CY et al (1993) Studies of anisotropy mechanisms in polyphosphate-treated magnetic iron oxide particles. J Magn Magn Mater 120:129–135
57. Tronc E, Ezzir A, Cherkaoui R et al (2000) Surface-related properties of γ-Fe_2O_3 nanoparticles. J Magn Magn Mater 221:63–79
58. Kolen'ko YV, Bañobre-López M, Rodríguez-Abreu C et al (2014) Large-scale synthesis of colloidal Fe_3O_4 nanoparticles exhibiting high heating efficiency in magnetic hyperthermia. J Phys Chem C 118:8691–8701
59. Tanimoto A, Kuribayashi S (2006) Application of superparamagnetic iron oxide to imaging of hepatocellular carcinoma. Eur J Radiol 58:200–216
60. Gupta AK, Wells S (2004) Surface-modified superparamagnetic nanoparticles for drug delivery: preparation, characterization, and cytotoxicity studies. IEEE Trans Nanobiosci 3:66–73
61. Firth JA (2002) Endothelial barriers: from hypothetical pores to membrane proteins. J Anat 200:541–548
62. Hirano A, Matsui T, Pathol H (1975) Vascular structures in brain tumors. Hum Pathol 6:611–621
63. Nandwana V, Elkins KE, Poudyal N (2007) Size and shape control of monodisperse FePt nanoparticles. J Phys Chem C 111:4185–4189
64. Sun SH, Zeng H, Robinson DB et al (2004) Monodisperse MFe_2O_4 (M = Fe, Co, Mn) nanoparticles. J Am Chem Soc 126:273–279
65. Xie J, Yan CZ, Zhang Y et al (2013) Shape evolution of "multibranched" Mn–Zn Ferrite nanostructures with high performance: a transformation of nanocrystals into nanoclusters. Chem Mater 25:3702–3709
66. Zeng H, Rice PM, Wang SX (2004) Shape-controlled synthesis and shape-induced texture of $MnFe_2O_4$ nanoparticles. J Am Chem Soc 126:11458–11459
67. Bao NZ, Shen LM, An W et al (2009) Formation mechanism and shape control of monodisperse magnetic $CoFe_2O_4$ nanocrystals. Chem Mater 21:3458–3468
68. Zhao ZH, Zhou ZJ, Bao JF et al (2013) Octapod iron oxide nanoparticles as high-performance T_2 contrast agents for magnetic resonance imaging. Nat Commun 4(2266):1–7
69. Agrawal A, Min DH, Singh N et al (2009) Functional delivery of siRNA in mice using dendriworms. ACS Nano 3:495–504
70. Pantarotto D, Singh R, McCarthy D et al (2004) Functionalized carbon nanotubes for plasmid DNA gene delivery. Angew Chem Int Ed 43:5242–5246
71. Bao L, Low WL, Jiang J et al (2012) Colloidal synthesis of magnetic nanorods with tunable aspect ratios. J Mater Chem 22:7117–7120

72. Hugounenq P, Levy M, Alloyeau D et al (2012) Iron oxide monocrystalline nanoflowers for highly efficient magnetic hyperthermia. J Phys Chem C 116:15702–15712
73. Bao NZ, Shen LM, Wang YH et al (2009) Controlled growth of monodisperse self-supported superparamagnetic nanostructures of spherical and rod-like $CoFe_2O_4$ nanocrystals. J Am Chem Soc 131:12900–12901
74. Hu M, Jiang JS (2010) Non-classical crystallization controlled by centrifugation. CrystEngComm 12:3391–3393
75. Wei YH, Klajn R, Pinchuk AO (2008) Synthesis, shape control, and optical properties of hybrid Au/Fe_3O_4 “nanoflowers”. Small 4:1635–1639
76. Wang LY, Park HY, Lim SII et al (2008) Core@shell nanomaterials: gold-coated magnetic oxide nanoparticles. J Mater Chem 18:2629–2635
77. Zhang J, Huang F, Lin Z (2009) Progress of nanocrystalline growth kinetics based on oriented attachment. Nanoscale 2:18–34
78. Jang JT, Nah H, Lee JH et al (2009) Critical enhancements of MRI contrast and hyperthermic effects by dopant-controlled magnetic nanoparticles. Angew Chem Int Ed 48:1234–1238
79. Wang LY, Wang X, Luo J et al (2010) Core-shell-structured magnetic ternary nanocubes. J Am Chem Soc 132:17686–17689
80. Lee JH, Jang JT, Choi JS et al (2011) Exchange-coupled magnetic nanoparticles for efficient heat induction. Nat Nanotechnol 6:418–422
81. Habib AH, Ondeck CL, Chaudhary P et al (2008) Evaluation of iron-cobalt/ferrite core shell nanoparticles for cancer thermotherapy. J Appl Phys 103:07A307
82. Fortin JP, Wilhelm C, Servais J et al (2007) Size-sorted anionic iron oxide nanomagnets as colloidal mediators for magnetic hyperthermia. J Am Chem Soc 129:2628–2635
83. Zeng H, Li J, Liu J et al (2002) Exchange-coupled nanocomposite magnets by nanoparticle self-assembly. Nature 420:395–398
84. Mornet S, Vasseur S, Grasset F et al (2004) Magnetic nanoparticle design for medical diagnosis and therapy. J Mater Chem 14:2161–2175
85. Karakoti AS, Das S, Thevuthasan S et al (2011) PEGylated inorganic nanoparticles. Angew Chem Int Ed 50:1980–1994
86. Howard MD, Jay M, Dziublal TD et al (2008) PEGylation of nanocarrier drug delivery systems: state of the art. Nanotechnology 4:133–148
87. Li Z, Wei L, Gao MY et al (2005) One-pot reaction to synthesize biocompatible magnetite nanoparticles. Adv Mater 17:1001–1005
88. Amstad E, Zurcher S, Mashaghi A et al (2009) Surface functionalization of single superparamagnetic iron oxide nanoparticles for targeted magnetic resonance imaging. Small 5:1334–1342
89. Gu L, Shen Z, Feng C et al (2008) Synthesis of PPEGMEA-g-PMAA densely grafted double hydrophilic copolymer and its use as a template for the preparation of size-controlled superparamagnetic Fe_3O_4/polymer nano-composites. J Mater Chem 18:4333–4340
90. Larsen EKU, Nielsen T, Wittenborn T et al (2009) Size-dependent accumulation of PEGylated silane-coated magnetic iron oxide nanoparticles in murine tumors. ACS Nano 3:1947–1951
91. Solin N, Kjellgren J, Szabo KJ et al (2004) Pincer complex-catalyzed allylation of aldehyde and imine substrates via nucleophilic η^1-allyl palladium intermediates. J Am Chem Soc 126:7026–7033
92. Sun C, Sze R, Zhang MQ et al (2006) Folic acid-PEG conjugated superparamagnetic nanoparticles for targeted cellular uptake and detection by MRI. J Biomed Mater Res Part A 78A:550–557
93. Chen K, Xie J, Xu HY et al (2009) Triblock copolymer coated iron oxide nanoparticle conjugate for tumor integrin targeting. Biomaterials 30:6912–6919
94. Deng JG, Ding XB, Zhang WH et al (2002) Magnetic and conducting Fe_3O_4-cross-linked polyaniline nanoparticles with core-shell structure. Polymer 43:2179–2184
95. Xu XL, Friedman G, Humfeld KD et al (2001) Superparamagnetic photonic crystals. Adv Mater 13:1681–1684

96. Vestal CR, Zhang ZJ (2002) Atom transfer radical polymerization synthesis and magnetic characterization of $MnFe_2O_4$/polystyrene core/shell nanoparticles. J Am Chem Soc 124:14312–14313
97. Huh YM, Jun YW, Song HT et al (2005) In vivo magnetic resonance detection of cancer by using multifunctional magnetic nanocrystals. J Am Chem Soc 127:12387–12391
98. Hayashi K, Nakamura M, Sakamoto W et al (2013) Superparamagnetic nanoparticle clusters for cancer theranostics combining magnetic resonance imaging and hyperthermia treatment. Theranostics 3:366–376
99. Mulder WJM, Strijkers GJ, van Tilborg GAF et al (2006) Lipid-based nanoparticles for contrast-enhanced MRI and molecular imaging. NMR Biomed 19:142–164
100. Gonzales M, Krishnan KM (2005) Synthesis of magnetoliposomes with monodisperse iron oxide nanocrystal cores for hyperthermia. J Magn Magn Mater 293:265–270
101. Namiki Y, Namiki T, Yoshida H et al (2009) A novel magnetic crystal-lipid nanostructure for magnetically guided in vivo gene delivery. Nat Nanotechnol 4:598–606
102. Amstad E, Kohlbrecher J, Muller E et al (2011) Triggered release from liposomes through magnetic actuation of iron oxide nanoparticle containing membranes. Nano Lett 11:1664–1670
103. Katagiri K, Nakamura M, Koumoto K et al (2010) Magnetoresponsive smart capsules formed with polyelectrolytes, lipid bilayers and magnetic nanoparticles. ACS Appl Mater Inter 2:768–773
104. Namiki Y, Fuchigami T, Tada N et al (2011) Nanomedicine for cancer: lipid-based nanostructures for drug delivery and monitoring. Acc Chem Res 44:1080–1093
105. Tong S, Hou SJ, Zheng ZK et al (2010) Coating optimization of superparamagnetic iron oxide nanoparticles for high T_2 relaxivity. Nano Lett 10:4607–4613
106. Xie J, Zhang Y, Yan CY et al (2014) High-performance PEGylated MneZn ferrite nanocrystals as a passive-targeted agent for magnetically induced cancer theranostics. Biomaterials 35:9126–9136
107. Gu L, Fang RH, Sailor MJ et al (2012) In vivo clearance and toxicity of monodisperse iron oxide nanocrystals. ACS Nano 6:4947–4954
108. Yu H, Chen M, Rice PM et al (2005) Dumbbell-like bifunctional Au-Fe_3O_4 nanoparticles. Nano Lett 5:379–382
109. Xu ZC, Hou YL, Sun SH (2007) Magnetic Core/Shell Fe_3O_4/Au and Fe_3O_4/Au/Ag nanoparticles with tunable plasmonic properties. J Am Chem Soc 129:8698–8699
110. Wang LY, Luo G, Fan Q et al (2005) Monodispersed core-shell Fe_3O_4@Au nanoparticles. J Phys Chem B 109:21593–21601
111. Goon IY, Lai LMH, Lim M et al (2009) Fabrication and dispersion of gold-shell-protected magnetite nanoparticles: systematic control using polyethyleneimine. Chem Mater 21:673–681
112. Bao J, Chen W, Liu TT et al (2007) Bifunctional Au-Fe_3O_4 nanoparticles for protein separation. ACS Nano 1:293–298
113. Lu Y, Yin Y, Mayers BT et al (2002) Modifying the surface properties of superparamagnetic iron oxide nanoparticles through a sol–gel approach. Nano Lett 2:183–186
114. Santra S, Tapec R, Theodoropoulou N et al (2001) Synthesis and characterization of silica-coated iron oxide nanoparticles in microemulsion: the effect of nonionic surfactants. Langmuir 17:2900–2906
115. Yi DK, Lee SS, Papaefthymiou GC et al (2006) Nanoparticle architectures templated by SiO_2/Fe_2O_3 nanocomposites. Chem Mater 18:614–619
116. Ung T, Liz-MarzXn LM, Mulvaney P (1998) Controlled method for silica coating of silver colloids. Influence of coating on the rate of chemical reactions. Langmuir 14:3740–3748
117. Geng J, Jefferson DA, Johnson BFG et al (2004) Direct conversion of iron stearate into magnetic Fe and Fe_3C nanocrystals encapsulated in polyhedral graphite cages. Chem Commun 2442–2443

118. Lu AH, Li W, Matoussevitch N et al (2005) Highly stable carbon-protected cobalt nanoparticles and graphite shells. Chem Commun 98–100
119. Taboada E, Rodríguez E, Roig A et al (2007) Relaxometric and magnetic characterization of ultrasmall iron oxide nanoparticles with high magnetization evaluation as potential *T1* magnetic resonance imaging contrast agents for molecular imaging. Langmuir 23:4583–4588
120. Cheon J, Lee JH (2008) Synergistically integrated nanoparticles as multimodal probes for nanobiotechnology. Acc Chem Res 41:1630–1640
121. Jun YW, Huh YM, Choi JS et al (2005) Nanoscale size effect of magnetic nanocrystals and their utilization for cancer diagnosis *via* magnetic resonance imaging. J Am Chem Soc 127:5732–5733
122. Weissleder R, Moore A, Mahmood U et al (2000) In vivo magnetic resonance imaging of transgene expression. Nat Med 6:351–354
123. Artemov D, Bhujwalla ZM, Bulte JW (2004) Magnetic resonance imaging of cell surface receptors using targeted contrast agents. Curr Pharm Biotechnol 2:165–172
124. Na HB, Song IC, Hyeon T (2009) Inorganic nanoparticles for MRI contrast agents. Adv Mater 21:2133–2148
125. Kim T, Murakami T, Hori M et al (2009) Effect of superparamagnetic iron oxide on tumor-to-liver contrast at *T2**-weighted gradient-echo MRI: comparison between 3.0T and 1.5T MR systems. J Magn Reson Imaging 29:595–600
126. Liu DF, Wu W, Ling JJ et al (2011) Effective PEGylation of iron oxide nanoparticles for high performance in vivo cancer ima*ging*. Adv Funct Mater 21:1498–1504
127. Lee N, Choi Y, Lee Y et al (2012) Water-dispersible ferrimagnetic iron oxide nanocubes with extremely high *r2* relaxivity for highly sensitive in vivo MRI of tumors. Nano Lett 12:3127–3131
128. Hu FQ, Wei L, Zhou Z et al (2006) Preparation of biocompatible magnetite nanocrystals for in vivo magnetic resonance detection of cancer. Adv Mater 18:2553–2556
129. Stone R, Willi T, Rosen Y et al (2011) Targeted magnetic hyperthermia. Ther Deliv 2:815–838
130. Walter A, Billotey C, Garofalo A et al (2014) Mastering the shape and composition of dendronized iron oxide nanoparticles to tailor magnetic resonance imaging and hyperthermia. Chem Mater 26:5252–5264
131. Maier-Hauff K, Rothe R, Scholz R et al (2007) Intracranial thermotherapy using magnetic nanoparticles combined with external beam radiotherapy: results of a feasibility study on patients with glioblastoma multiforme. Neuro Oncol 81:53–60
132. Maier-Hauff K, Ulrich F, Nestler D et al (2011) Efficacy and safety of intratumoral thermotherapy using magnetic iron-oxide nanoparticles combined with external beam radiotherapy on patients with recurrent glioblastoma multiforme. J Neuro Oncol 103:317–324
133. Trana N, Webster TJ (2010) Magnetic nanoparticles: biomedical applications and challenges. J Mater Chem 20:8760–8767
134. Jordan A, Scholz R, Wust P et al (1997) Effects of magnetic fluid hyperthermia (MFH) on C_3H mammary carcinoma in vivo. Int J Hyperthermia 13:587–605
135. Hilger I, Rapp A, Greulich KO et al (2005) Assessment of DNA damage in target tumor cells after thermoablation in mice. Radiology 237:500–506
136. Laurent S, Dutz S, Hafeli UO et al (2011) Magnetic fluid hyperthermia: focus on superparamagnetic iron oxide nanoparticles. Adv Colloid Interface Sci 166:8–23
137. Guardia P, Riccardo DC, Lartigue L et al (2012) Water-soluble iron oxide nanocubes with high values of specific absorption rate for cancer cell hyperthermia treatment. ACS Nano 6:3080–3091
138. Hergt R, Dutz S (2007) Magnetic particle hyperthermia-biophysical limitations of a visionary tumour therapy. J Magn Magn Mater 311:187–192
139. Gilchrist RK, Medal R, Shorey WD et al (1957) Selective inductive heating of lymph nodes. Ann Surg 146:596–606

140. Jordan A, Wust P, Faehling H et al (2009) Inductive heating of ferrimagnetic particles and magnetic fluids: physical evaluation of their potential for hyperthermia. Int J Hyperthermia 25:499–511
141. Johannsen M, Gneveckow U, Eckelt L et al (2005) Clinical hyperthermia of prostate cancer using magnetic nanoparticles: presentation of a new interstitial technique. Int J Hyperthermia 21:637–647
142. Lepock JR (2003) Cellular effects of hyperthermia: relevance to the minimum dose for thermal damage. Int J Hyperthermia 19:252–266
143. Thrall DE, Larue SM, Pruitt AF et al (2006) Changes in tumour oxygenation during fractionated hyperthermia and radiation therapy in spontaneous canine sarcomas. Int J Hyperthermia 22:365–373
144. Song CW, Park H, Griffin RJ et al (2001) Improvement of tumor oxygenation by mild hyperthermia. Radiat Res 155:515–528
145. Ingrid H, Robert H, Rudolf H et al (2002) Thermal ablation of tumors using magnetic nanoparticles: An in vivo feasibility study. Invest Radiol 37:580–586
146. Huang HS, Hainfeld JF (2013) Intravenous magnetic nanoparticle cancer hyperthermia. Int J Nanomed 8:2521–2532
147. Ren YY, Zhang HJ, Chen BA et al (2012) Multifunctional magnetic Fe_3O_4 nanoparticles combined with chemotherapy and hyperthermia to overcome multidrug resistance. Int J Nanomed 7:2261–2269
148. Bruners P, Hodenius M, Baumann M et al (2008) Magnetic thermal ablation using ferrofluids: influence of administration mode on biological effect in different porcine tissues. Cardiovasc Intervent Radiol 31:1193–1199
149. Elsherbini AA, Saber M, Aggag M et al (2011) Magnetic nanoparticle–induced hyperthermia treatment under magnetic resonance imaging. Imaging 29:272–280
150. Balivada S, Rachakatla RS, Wang H et al (2010) A/C magnetic hyperthermia of melanoma mediated by iron(0)/iron oxide core/shell magnetic nanoparticles: a mouse study. BMC Cancer 10:119–1–9
151. DeNardo SJ, DeNardo GL, Natarajan A et al (2007) Thermal dosimetry predictive of efficacy of 111 In-ChL6 nanoparticle AMF–induced thermoablative therapy for human breast cancer in mice. J Nucl Med 48:437–444
152. Gazeau F, Lévy M, Wilhelm C et al (2008) Optimizing magnetic nanoparticle design for nanothermotherapy. Nanomed 3:831–844
153. Daxiang Cui YH, Zhiming L, Song H et al (2009) Fluorescent magnetic nanoprobes for in vivo targeted imaging and hyperthermia therapy of prostate cancer. Nano Biomed Eng 1:61–74